NTNU
Norwegian University of
Science and Technology

Real time ultrasound simulation

Application to a medical training simulator

Lars Eirik Bø

Master of Science in Physics and Mathematics

Submission date: June 2008

Supervisor: Kristian Seip, MATH
Co-supervisor: Reidar Brekken, SINTEF Helse
Toril A. Nagelhus Hernes, SINTEF Helse

Norwegian University of Science and Technology
Department of Mathematical Sciences

Problem Description

An ultrasound simulation method has previously been developed and implemented in MATLAB. The method produces simulated ultrasound images in real time based on information in a three-dimensional CT data set, taking advantage of the qualitative, visual similarities between CT and ultrasound images. This master's project aims at improving the simulations by exploiting the quantitative information available in the CT data in combination with physical models of ultrasound imaging. The project contains the following sub tasks:

- A theoretical description and analysis of the relationship between CT and ultrasound imaging.

- Development of a model describing typical features of ultrasound imaging, such as reflections, scattering, absorption and noise, in terms of information extracted from CT images.

- Implementation of the simulation model in MATLAB.

- Comparison of simulated and true ultrasound images.

Assignment given: 15. January 2008
Supervisor: Kristian Seip, MATH

Preface

This master's thesis concludes my studies for the Master's Degree in Physics and Mathematics at the Norwegian University of Science and Technology (NTNU). The work on the thesis was carried out at SINTEF Health Research during the spring of 2008, and it forms part of the project "Ultrasound simulator - helping save lives" (USSim) which is a collaboration between Laerdal Medical AS, SINTEF, NTNU and St. Olavs Hospital. It has been a source of motivation to have a problem at hand with direct implications to a larger project. I am also privileged to have had the opportunity to work closely with the skilled and knowledgeable coworkers at SINTEF who constantly have been eager to help.

I must first of all thank my two supervisors at SINTEF, Reidar Brekken and Toril A. Nagelhus Hernes, who have helped me and guided me all the way from the formulation of the problem to the final conclusion. An additional thanks goes to all the participants of the USSim project for including me in their group and showing interest in my work. I am also grateful to Rune Hansen for his expert guidance in the world of ultrasound imaging and to professor Kristian Seip who has been my contact at the Department of Mathematical Sciences. Finally, i must thank the rest of the Department of Medical Technology at SINTEF for discussions, advice and help and for sharing their workplace with me. The occasional football tournament made all the difference.

Lars Eirik Bø
Trondheim, June 10, 2008

Summary

As ultrasound technology today finds new applications and becomes available to more and more users, the demand for good training procedures and material increases. This has motivated a research project aimed at developing an ultrasound simulator for training purposes. As a part of the project, a simulation method has previously been developed capable of producing artificial ultrasound images in real time based on three-dimensional CT data. However, the method takes advantage mainly of the qualitative, visual similarities between CT and ultrasound images. This master's project investigates the possibility of exploiting the quantitative information available in the CT data in combination with physical models of ultrasound imaging. The aim is to enhance the realism of the simulations while still retaining its real time performance.

As a part of the investigations, a new simulation method has been implemented in MATLAB. The method estimates acoustic impedance values from CT numbers, and combines this with physical models connecting the estimates to effects fundamental to ultrasound image formation, mainly reflection and scattering. Effects such as absorption and electronic noise are also added to the simulation.

Comparison between simulated images and corresponding true ultrasound images shows that reflections and shadows are quite well reproduced by the new method. The simulated artifacts are also slightly more realistic than those produced by the previous method, indicating that such computations can benefit from taking quantitative information into account. The attempt at computing the scattering of ultrasound, on the other hand, is not successful. It is likely that the information contained in the CT images is insufficient to predict such effects. Alternative methods should therefore be considered for this purpose.

Contents

Chapter 1

Introduction

1.1 Medical simulators

Simulators for education and training purposes have throughout the last decades become more and more common and are today used within a wide range of areas [1]. They are usually applied when training on actual equipment is too expensive, too dangerous or in other ways inconvenient. Flight simulators, which have been a part of training procedures for pilots since the 1950s, is a typical example of this [2].

The first patient simulator mannequins for training of medical personnel were developed in the late 1960s, and they have since become increasingly more popular and more advanced. Today, such simulators are being used by one-third of all medical schools in the USA and by hundreds of medical institutions all over the world [3]. There they are being utilized in helping students and professionals learning everything from basic skills to the treatment of complex and infrequently occurring clinical problems and procedures. These patient simulators have a large number of features including palpable pulses, speakers broadcasting heart and lung sounds, advanced airway and lung models and actuators allowing standard medical equipment such as electrocardiographs and blood pressure monitors to be connected to the mannequin. A typical high-end model is shown in figure 1.1.

Another kind of medical simulators has become more common the last decades, particularly due to the advances within computer technology. These simulators are either based completely on virtual reality using computer simulations, or they combine this with real medical images or physical objects such as mannequins, organ models or surgical tools. Using such methods, surgical simulators have been developed to train a wide range of surgical procedures [2]. Some imaging techniques, where the interpretation of the images is dependent on the operator's manipulation of a sensor or a camera, also lend themselves to these kinds of simulations. This is the case for both endoscopy and ultrasound, and simulators have been developed for both of these applications [4, 5].

There are several advantages of using simulators in medical training, and some of them are outlined by Good [3]. First of all, the training program may be adapted to the students' needs rather than to the patients. Simulators also allow students to train without fear of mistakes since these do not have

Figure 1.1: The patient simulator SimMan 3G from Laerdal Medical AS (Stavanger, Norway).

any consequences for real patients. From an instructor's point of view, simulators provide a standardized environment facilitating objective assessment of the students' performance. Moreover, many simulators give immediate feedback reducing the need for tutoring and allowing collaborative learning. The most obvious disadvantage of simulator training is the limitation with respect to realism. Such training can therefore never fully replace training on real patients. Moreover, advanced simulators are often expensive, and the costs of establishing a simulator-based training program may therefore be considerable.

1.2 Ultrasound imaging and simulation

Ultrasound imaging is a medical imaging modality which uses high frequency sound waves to image structures within the body [6]. The sound waves are transmitted into the body, and the echo consisting of reflected and scattered components of the initial waves is recorded. This echo depends on the characteristics of the propagation medium, i.e. the body tissue, and thus contains information about these characteristics. This information can then to a certain degree be extracted from the echo through signal processing and displayed in one of many ways depending on which part of the information is relevant to the user.

The most common type of ultrasound imaging is the pulse echo amplitude imaging. Here a short ultrasound pulse is transmitted and the amplitude of the echo is recorded. Based on the direction of the beam and the time it takes for the echo to return to the transducer, the location of the source of each different part of the echo is determined. There are several different ways to display this information, referred to as different modes [7]. The most common mode is the B-mode, which stands for brightness mode. Here, beams are sent out in several directions so that an entire two-dimensional sector is scanned. This is referred to as the scan sector. Intensity data are then displayed as different shades of gray in two-dimensional space, and the image is updated in real time.

The development of medical ultrasound imaging was originally based on advances within radar and sonar technology made during the last world war.

The first cross-sectional images were produced as early as 1950, and a lot of research was performed in the area during the following decades [8]. However, the breakthrough of the technology came first as the electronic instrumentation evolved from vacuum tubes to integrated circuits. Around 1970, real time, two-dimensional imaging was introduced, and this finally lead to ultrasound becoming a well accepted diagnostic imaging modality [9]. Today, ultrasound imaging is used within numerous medical specialities to image nearly all soft tissue structures in the body [10]. It provides fast and safe diagnosis of a large number of conditions, and because it involves no ionizing radiation, it is the preferred method of imaging whenever it can give useful clinical information [11]. Recent advances have also resulted in improved image quality as well as smaller and more portable equipment. This has made new applications possible, e.g. in trauma situations where small ultrasound scanners can be brought to the site for fast and accurate diagnosis [12]. At the same time, the cost of the equipment is decreasing making it available to more and more users.

However, a challenge with this technology is that it is very operator-dependent and requires a large amount of training. One obvious reason for this is the low quality of the images compared to other medical imaging modalities, which makes the interpretation of the images difficult. The interpretation is also highly dependent on the movements of the ultrasound probe [5]. It usually requires a mental fusion of two-dimensional images combined with information of probe position and motion to get information about shape and motion of structures within the body. These requirements make ultrasound imaging particularly apt for simulation training, and several simulators for this purpose have been developed throughout the last decade [5]. The complexity of these simulators vary a lot, from simple computer applications to realistic systems incorporating a mannequin and a dummy ultrasound scanner, and several different clinical applications have been implemented.

A core technology in ultrasound simulators is the methods producing virtual ultrasound images for display. In current simulators, these are mostly based on prerecorded, three-dimensional sets of ultrasound images from patients. However, collecting such data sets is a tedious process which is inconvenient to the patients and not feasible in all settings. This is e.g. the case in trauma situations, where time is of the essence. The data sets also require a considerable amount of preprocessing before they can be used in the simulators. Alternative technologies have therefore also been developed, including simulations based on data sets from other imaging modalities. This is further described in section 2.1.

1.3 The USSim project

This master's thesis forms part of the research project "Ultrasound simulator - helping save lives" (USSim) which was started in 2006 as a collaboration between the company Laerdal Medical AS in Stavanger, SINTEF Health Research, the Norwegian University of Science and Technology (NTNU) and St. Olavs Hospital in Trondheim. It was motivated by clinical demands for new diagnostic imaging technology in combination with the significant advances which have taken place within the area of ultrasound imaging in recent years. As mentioned have these advances opened up for new applications and increased availability, but in

order to fully exploit this, good training methods are required. The objective of the USSim project is therefore to develop a simulator imitating ultrasound examination procedures as realistically as possible.

The first phase of the project focuses on the application of B-mode imaging in trauma situations. As illustrated in figure 1.2, the simulator is planned to consist of a life-sized mannequin, a dummy ultrasound probe with an integrated positioning system and an image simulator producing virtual ultrasound images. A first prototype of such a system was presented in the spring of 2007. To facilitate easy access to a wide selection of realistic cases, the simulations are to be based on CT data from patients collected in clinical settings. The overall goal is to produce a system which can optimize the usage and interpretation of ultrasound imaging and thereby improve the quality and efficiency of health care.

1.4 Objectives

The prototype ultrasound simulator developed in the USSim project incorporates a simulation method producing simulated ultrasound images in real time. The simulations are based on information in a three-dimensional CT data set, taking advantage of the qualitative, visual similarities between CT and ultrasound images. The objective of this master's project is to investigate the possibility of exploiting the quantitative information available in the CT data in combination with physical models of ultrasound imaging in order to enhance the realism of the simulations.

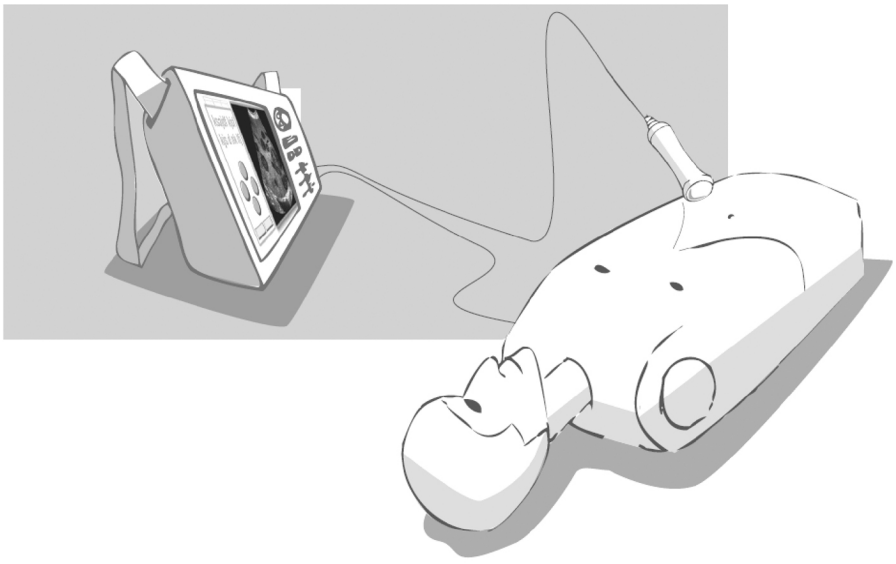

Figure 1.2: A sketch of the proposed USSim system consisting of a life-sized mannequin, a dummy ultrasound probe with an integrated positioning system and an image simulator producing virtual ultrasound images.

1.5 Overview of the report

Chapter 2 of this report starts by giving a general introduction to ultrasound simulation, before presenting some essential CT and ultrasound theory. This presentation is aimed at providing the physical models needed for the following simulations. A detailed description of the developed simulation method and its implementation in MATLAB is given in chapter 3, where the experimental setup used to evaluate the method is also introduced. Chapter 4 presents some typical images produced by the new simulation method and by the previously implemented method together with corresponding, real ultrasound images. In chapter 5, the different parts of the simulation method are discussed in light of the presented results, and possible future work is suggested based on this discussion.

Please note that parts of the background material in chapters 1 and 2 are taken from a project report written by the candidate in the fall of 2007 [13].

Chapter 2

Theory

The prototype ultrasound simulator developed in the USSim project incorporates an image simulation method producing artificial ultrasound images. The simulations are based on information in CT data sets, and a thorough understanding of both ultrasound and CT imaging is thus required in order to improve the method. This chapter should provide a simple, but well founded, description of the physical properties imaged by CT and how these properties influence the formation of ultrasound images. First, a general introduction to the simulation of ultrasound is given before turning to the physics of CT and ultrasound imaging.

2.1 Ultrasound simulation methods

Computer simulations of ultrasound have become more and more common throughout the last couple of decades [14, 15]. It has primarily been used as a tool within research and development, but more recently other applications have also appeared. The simulation methods which have been developed may be divided into two main categories which have been referred to as the *generative approach* and the *interpolation approach* [16]. The generative approach is the traditional way of simulating ultrasound images, while the interpolation approach and related methods have arisen from the need to simulate ultrasound images in real time, specifically for use in training simulators.

Generative approach

The generative approach is based on physical models of wave propagation and signal processing. Using these models the entire image formation, from the generated electrical pulse via the acoustical sound wave to the received and displayed signal can be computed. An ultrasound imaging system can be divided into three different parts:

- Electrical pathway and transducer.
- Acoustic field, wave propagation and scattering.
- Propagation medium.

Applying the generative approach to the simulation of such a system, these areas may be simulated separately using specialized methods.

Simulation of electrical circuits has been done ever since the simulation programme SPICE was developed in the mid seventies, and this programme has since become an industry standard [17]. This and similar tools can readily be applied to the electrical part of the ultrasound system. When it comes to the conversion of the electrical signal into an acoustical signal as it occurs in the piezoelectric transducers, this can be implemented by means of an equivalent circuit. This has been done by several authors, the most notable being Mason's model and the KLM model [18, 19]. These models are however limited to one-dimensional approximations which are not always applicable, and in order to model the real three-dimensional geometry of the transducers one usually has to turn to more complicated finite element analysis [14].

The problem of finding the sound field generated by a given transducer is a much studied one, and the efforts to solve it can be traced back to the famous, British physicist lord Rayleigh [20]. In the context of ultrasound simulation, the most famous solution method was invented by Tupholme [21] and Stepanishen [22, 23] and further developed by Jensen and Svendsen [24]. The method assumes linear wave propagation and applies linear system theory, modelling the interaction between the ultrasound wave and the propagation medium as an impulse response. The simulation software Field II, also developed by Jensen [25], is based on this approach and is in widespread use among ultrasound scientists today. In order to take higher order effects into account, more advanced, numerical solvers must be utilized such as finite elements methods or spectral methods [26]. These methods can be adapted to accommodate both non-linear wave propagation and heterogeneous propagation media, and the initial pulse can be propagated either in the time domain or in the spatial domain depending on the available initial conditions and the effects which are to be studied [27].

Good models describing the generation, propagation and scattering of ultrasound waves is not sufficient to achieve a realistic simulation of ultrasound image formation. Proper computer phantom modeling of the propagation medium is also essential, and in the case of medical imaging this implies detailed modeling of human anatomy and function [28, 29]. The form these models take depends on the underlying wave models, and this, together with the available computational power, largely determines the degree of complexity and realism which is possible to achieve.

One central disadvantage of simulation methods using the generative approach is that they tend to be time-consuming. A lot of effort has therefore been made to develop fast simulations for various application [30, 31]. The issue of efficiency is particularly challenging when it comes to simulators for training purposes. In order to provide a realistic experience for the operator, such a simulator should produce images at frame rates comparable to those of a proper ultrasound scanner operating in real time. This is usually between 10 and 30 frames per second [6].

There have been attempts at methods that deal with real time constraints using the generative approach. Varlet [32] presents a method using a technique from geometrical optics known as ray tracing. Here, the wave propagation is modeled as rays of light emitted from a source, and the propagated and reflected wave field is calculated by considering the interaction between each ray and optical surfaces in the propagating medium. This method can be adapted

to sound waves and produces images in real time showing tissue boundaries. However, the simulation produces no speckle or side lobe noise which is characteristic of ultrasound images. Another method developed by Abkai et al. [33] simulates intravascular ultrasound (IVUS) applying a system based approach [34]. It takes advantage of the approximate radial symmetry of the medium, i.e. the blood vessel, and the simple spatial impulse response of the single element IVUS transducer to achieve real time performance.

Interpolation approach

The interpolation approach, on the other hand, was developed specifically for use in training simulators where computational efficiency is essential and the goal is realistic images. Rather than physical models of wave propagation, this approach uses a more or less dense 3D volume of actual, prerecorded ultrasound images [16]. Such images will have some view dependent features which depend on the position of the probe during recording, such as shadows and intensity variations, but these may to some degree be removed by means of image processing. One may then simulate images recorded from any position by extracting the corresponding plane from the volume and include the appropriate view dependent features, a process which may be performed very quickly [35]. The new image is hence an interpolation of image data from the prerecorded images constituting the 3D volume.

This approach has been implemented several times and has lead to simulators such as the UltraSim [35] and the SONOSim3D [36]. There have also been efforts to incorporate dynamic effects in the simulations. Tissue deformation due to probe pressure has been implemented by distorting the interpolated images [16], and a simulator for echocardiography has been made using a dynamic 3D volume of ultrasound images [37].

An alternative to using prerecorded ultrasound data in these kinds of simulations is to use 3D data sets from other imaging modalities such as magnetic resonance imaging (MRI) or computed tomography (CT) [38, 39]. Such data sets are easier to collect than 3D ultrasound data. Moreover, they do not have any view dependent features, which reduces the need for preprocessing. The obvious challenge is that these data lack many of the characteristics of real ultrasound images, and they must hence be manipulated during simulation in order to produce realistic images.

This last method is the one implemented in the prototype of the USSim project, and since it depends on the relationship between CT data and ultrasound imaging, the next two sections are devoted to these imaging modalities.

2.2 CT imaging

Computed tomography (CT) is an imaging modality capable of producing high-resolution, three-dimensional images of the insides of objects. Since its invention in the 1970s, it has become one of the corner stones within medical imaging, drastically reducing the need for exploratory surgery [6]. CT employs X-rays, which is electromagnetic radiation at frequencies just above ultraviolet light, i.e. in the range $3 \cdot 10^{17} - 5 \cdot 10^{19}$ Hz [40]. Such radiation interacts with matter in different ways, and as an X-ray passes through an object this interaction may

cause an attenuation of the ray. However, since the interaction, and therefore also the attenuation, varies with different kinds of matter, the level of attenuation contains information about the composition of the traversed matter. This information can thus be used to produce an image. The word tomography is a compound of the Greek words for slice, tomos, and drawing, graphikos, and stems from the way the CT images are collected slice by slice.

In traditional X-ray imaging, several X-rays are transmitted into the object in question from one side [6]. On the other side, detectors measure the intensities of the transmitted rays having passed through the object. Each of these measurements can then be used to determine the total attenuation of the X-ray along a path from the emitting radiation source to the corresponding detector. The resulting value can be considered a projection of the attenuating properties of the medium along this path onto the detector. By measuring the transmitted X-rays at closely spaced points in a given plane in space, a two-dimensional projection image of the three-dimensional object can thus be created. This is illustrated in figure 2.1(a). CT imaging is also based on projections. However, in order to produce a three-dimensional image, information about the attenuating properties at distinct points in space is required. In CT, this information is obtained by moving the radiation sources and the detectors around the object as shown in figure 2.1(b), thus acquiring a number of one-dimensional projections from the same area. As the sources are moved once around the object in a circular motion, the emitted X-rays slice through the object, and the collected projections all stem from this slice. The resulting information allows the attenuation properties of a large number of points within the slice to be computed. By repeating this for several adjacent slices, a three-dimensional image can be produced.

The photons in X-rays interact with the atoms of matter in different ways, and the interactions can be devided into scattering and absorption processes [6]. The nature of these interactions depends both on the elemental composition of the matter and on the energy content of the radiation, measured as energy per photon E. For the energies applied in diagnostic radiology and nuclear medicine, there are three main kinds: Rayleigh scattering, Compton scattering and photoelectric absorption, all of which contribute to the attenuation of the X-rays. This attenuation is usually characterized in terms of the linear attenuation coefficient μ which is defined as the fraction of photons removed from a monoenergetic beam of X-rays per unit thickness of material. That a beam is monoenergetic means that all of its photons have the same energy E, and for such beams the simple relationship [6]

$$N = N_0 e^{-\mu x}$$

applies, where N_0 is the number of incident photons transmitted into the material, N is the number of photons transmitted out on the other side and x is the thickness of the material. The contributions to the attenuation by the different kinds of interaction can similarly be characterized in terms of the coefficients μ_{Rayleigh}, μ_{Compton} and $\mu_{\text{photoelectric}}$, and μ is then the sum of these.

The values of μ measured in CT imaging will usually vary somewhat from scanner to scanner [41]. To allow for comparison between different machines, the values are therefore returned as normalized CT numbers, also known as

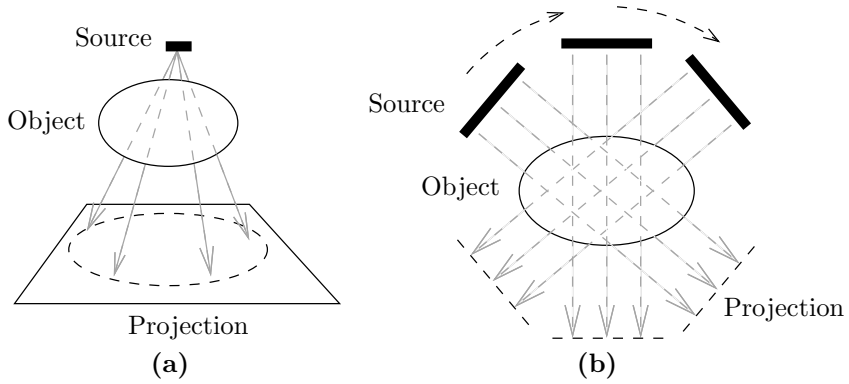

Figure 2.1: (a) Generation of a two-dimensional projection image using X-rays, and (b) acquisition of several one-dimensional projections of a single slice to produce a CT image.

Hounsfield units, given as

$$h(\mathbf{r}) = 1000 \left(\frac{\mu(\mathbf{r})}{\mu_{\text{water}}} - 1 \right),$$

where μ_{water} is the attenuation coefficient of water measured by the specific scanner. The CT numbers range from -1000, which implies no attenuation, as in air, and usually up to about 1000. Water is by definition assigned a CT number of 0, and other typical CT numbers can be seen in figure 2.2 [42].

The X-rays used in CT imaging have an average energy of about 75 keV per photon [6]. For such radiation traversing human tissue, between 74% and 95% of the interaction is Compton scattering which means that the photons interact with the electrons in the outer shells of the atoms, ionizing the atoms and causing the photons to lose energy and change direction. The corresponding attenuation coefficient μ_{Compton} is proportional to the mass density ρ of the medium. It also depends on electron density ρ_{e}, but since this varies little between the constituents of human tissue, this dependence can mostly be ignored. The notable exception is hydrogen with a somewhat high electron density, and hydrogenous tissue, such as fat, will therefore cause a relatively strong attenuation. However, disregarding variations in ρ_{e}, the proportional relationship between μ_{Compton} and ρ implies an approximately linear relationship between ρ and CT number h. This relationship has been investigated e.g. by Schneider et al. [41] who measured mass density and CT numbers for different kinds of tissue and performed a statistical analysis of the correlation between these vari-

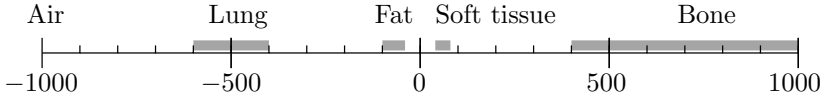

Figure 2.2: The scale of CT numbers or Hounsfield units. Typical range of different human tissues are indicated [42].

ables. By dividing the tissue in three groups they were able to identify a linear relationships on the form

$$\rho(h) = a_1 + a_2 h, \tag{2.1}$$

where the correlation parameters a_1 and a_2 depend on the group of tissue as shown in table 2.1. The resulting values for h are given in kg/m^3.

2.3 Ultrasound imaging

The sound waves applied in medical ultrasound imaging are longitudinal pressure waves with frequencies ranging from 2 to 40 MHz [7]. They are produced by a transducer which usually consists of an array of piezoelectric elements [43]. These elements vibrate when varying voltages are applied to them and thus create a joint sound wave or sound beam. By having the elements vibrate with different amplitudes and time delays it is possible to focus and steer this beam and thus optimize the signal received from the target area and attenuate the signal received from other areas. This is known as beam forming. Within medical imaging, ultrasound is primarily used to image biological soft tissues. These tissues can be modelled as fluids, and as such they possess the two properties which are necessary and sufficient for the propagation of pressure waves: elasticity and inertia, measured as compressibility κ and density ρ respectively [44]. A propagating wave can to a large degree be characterized in terms of these two variables, and other important parameters can be derived from them. Propagation speed c and acoustic impedance Z are examples of this, given as $c = \sqrt{1/\rho\kappa}$ and $Z = \sqrt{\rho/\kappa}$ respectively [7].

As for X-rays, the interactions between an ultrasound wave and the medium it propagates through can be divided into scattering and absorption processes [44]. Scattering implies that a part of the energy of the incident wave is converted into new waves with different properties than the original one, e.g. through reflection, whereas absorption is the transformation of acoustic wave energy into thermal energy in the medium. The predominant cause of both these processes is inhomogeneities in the propagation medium, i.e. spatial variations in the acoustic properties κ and ρ [45]. Since the echo utilized in ultrasound imaging consists of scattered components of the transmitted wave, these images are completely dependent on such inhomogeneities. The interaction processes also cause an attenuation of the transmitted wave, and thus limit the range of the imaging system. In soft tissues, acoustic absorption is responsible for more than 90% of this attenuation, while at interfaces between soft tissues and other substances a considerable part of the wave can be reflected and correspondingly attenu-

Table 2.1: Groups of tissue and corresponding correlation parameters a_1 and a_2. Inserting these parameters into (2.1), the mass density ρ can be computed based on CT number h [41].

Tissue group	CT Numbers h	a_1 [kg/m^3]	a_2 [kg/m^3]
Soft tissues	$-98 \leqslant h \leqslant 14$	1018	0.893
Dense soft tissues	$23 \leqslant h \leqslant 100$	1003	1.169
Skeletal tissues	$-22 \leqslant h \leqslant 1524$	1017	0.592

ated [7]. Areas causing particularly strong attenuation produce characteristic shadows in the images [6].

Mathematically, the behaviour of acoustic waves in soft tissue is a complicated matter, and it depends on highly detailed knowledge of the acoustic properties of the propagation medium, including κ and ρ. However, under quite general simplifying assumptions it is possible to derive a manageable wave equation describing the propagation of sound waves and their interaction with a heterogeneous propagation medium. The description presented here is principally based on the exposition by Insana and Brown [44]. They model soft tissue as an inhomogeneous continuum where the compressibility and density at equilibrium, denoted κ_e and ρ_e, are given as small, spatial variations $\Delta\kappa_\mathrm{e}(\mathbf{r})$ and $\Delta\rho_\mathrm{e}(\mathbf{r})$ around the characteristic average values κ_0 and ρ_0, i.e. $\kappa_\mathrm{e}(\mathbf{r}) = \kappa_0 + \Delta\kappa_\mathrm{e}(\mathbf{r})$ and $\rho_\mathrm{e}(\mathbf{r}) = \rho_0 + \Delta\rho_\mathrm{e}(\mathbf{r})$. Initially, they assume the medium to be without loss, thus neglecting acoustic absorption processes. However, since these processes are notable in soft tissue, this effect is included in the model at a later stage. They also adopt several other common simplifications, e.g. that the scattering of sound in the medium is relatively weak, known as the Born approximation, and that the speed of sound is independent of frequency within the considered range of frequencies, both of which are good approximations for biological soft tissues. By additionally neglecting heat flow within the medium and nonlinear effects, this model allows a four-dimensional, linear wave equation for the pressure field in the propagation media to be derived from only three basic laws of physics: the equation of continuity, Euler's equation and the equation of state. The result can be written [44]

$$\nabla^2 p - \frac{1}{c^2}\frac{\partial^2 p}{\partial t^2} = \gamma_\kappa(\mathbf{r})\frac{1}{c^2}\frac{\partial^2 p}{\partial t^2} + \nabla\cdot(\gamma_\rho(\mathbf{r})\nabla p) \tag{2.2}$$

where $p = p(\mathbf{r}, t)$ is the pressure, which is a function of space and time, and

$$\begin{aligned}
\gamma_\kappa(\mathbf{r}) &= (\kappa_\mathrm{e}(\mathbf{r}) - \kappa_0)/\kappa_0 = \Delta\kappa_\mathrm{e}(\mathbf{r})/\kappa_0,\\
\gamma_\rho(\mathbf{r}) &= (\rho_\mathrm{e}(\mathbf{r}) - \rho_0)/\rho_\mathrm{e}(\mathbf{r}) = \Delta\rho_\mathrm{e}(\mathbf{r})/\rho_\mathrm{e}(\mathbf{r}),\\
c^2 &= 1/(\rho_0\kappa_0).
\end{aligned}$$

(2.2) is a classical inhomogeneous wave equation with two source terms on the right hand side, both of which are due to fluctuations in κ and ρ, represented by the parameters γ_κ and γ_ρ. These terms are responsible for the scattering of the propagating wave and they are therefore commonly referred to as scattering sources [44]. The propagation speed c, on the other hand, is only dependent on ρ_0 and κ_0 and is hence constant. The equation is valid only within regions where these average properties can be considered to be relatively consistent. However, by dividing the propagation medium into areas with different average properties, i.e. different kinds of tissue, a separate wave equation can be solved for each area while matching the boundary conditions at the interfaces, and a description of the pressure field can thus be found for the entire medium.

The nature of the interaction between the ultrasound waves and inhomogeneities in the propagation medium largely depends on the spatial dimensions of the inhomogeneities [45]. Large, macroscopic interfaces, such as organ boundaries within the human body, cause a specular reflection and refraction of the wave, while smaller inhomogeneities with dimensions comparable to the wavelength of the ultrasound scatter the wave in all directions. Even though both

of these interactions are scattering processes in the sense described above, it is common to refer to them as reflection and scattering respectively. This convention is followed in the rest of this work. Rough interfaces, as most tissue boundaries are, lead to a combination of these two effects referred to as diffuse reflection [7]. Particles much smaller than the wavelength contribute very effectively to the acoustic absorption. The different kinds of interaction are illustrated in figure 2.3. In an ultrasound image, specular reflections appear as bright interfaces, whereas scattering is responsible for the shades of gray and patterns of the soft tissues.

Reflection and transmission

The specular reflections occurring at large interfaces conform with the law of reflection stating that the angle of reflection α_r, which is the angle between the reflected wave and the interface normal, equals the angle of incident α_i as shown in figure 2.3(a) [7]. Similarly, the angle of refraction α_t between the transmitted wave and the interface normal is determined by the relationship

$$\frac{\sin\alpha_\mathrm{i}}{\sin\alpha_\mathrm{t}} = \frac{c_1}{c_2}$$

known as Snell's law, where c_1 and c_2 are the wave velocities of the propagation media on each side of the interface. The fractions of the incident wave which are reflected and transmitted depend on the acoustic impedance Z of the media in question, defined as $Z = \rho c$. Assuming an incident wave with pressure amplitude p_i and corresponding reflected and transmitted waves with pressure amplitudes p_r and p_t, the ratios $R_p = p_\mathrm{r}/p_\mathrm{i}$ and $T_p = p_\mathrm{t}/p_\mathrm{i}$ are referred to as the reflection and transmission coefficients. These are given in terms of Z_1 and Z_2 as [7]

$$R_p = \frac{Z_2 - Z_1}{Z_2 + Z_1} \quad \text{and} \quad T_p = \frac{2Z_2}{Z_2 + Z_1}.$$

The intensity of a wave is defined as power per unit area, and in general this is proportional to the square of the pressure amplitude [7]. The ratios between the intensity I_i of the incident wave and the intensities I_r and I_t of the reflected

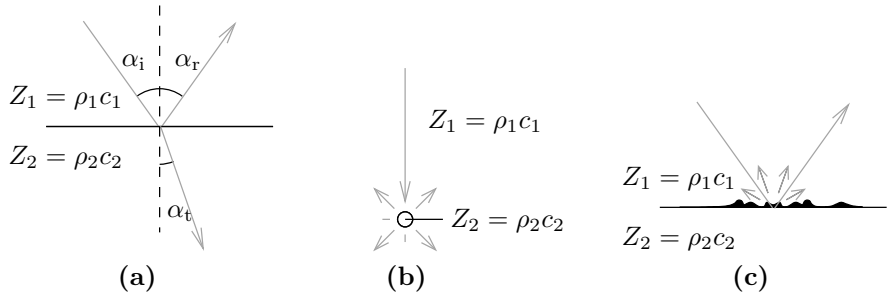

Figure 2.3: Schematic drawing illustrating (a) specular reflection and refraction, (b) scattering and (c) diffuse reflection. The illustration is adapted from Angelsen [7].

and transmitted waves are hence similarly given as

$$R_I = \left(\frac{Z_2 - Z_1}{Z_2 + Z_1}\right)^2 \quad \text{and} \quad T_I = 1 - R_I. \tag{2.3}$$

Here, the last expression follows from the conservation of energy dictating that $I_\mathrm{i} = I_\mathrm{r} + I_\mathrm{t}$, which implies $R_I + T_I = 1$. It is also worth noting that Z_1 and Z_2 are interchangeable in (2.3), making R_I and T_I symmetrical in the sense that both sides of a given interface reflect and transmit the same fraction of any incident energy.

Scattering

The scattering of ultrasound waves caused by small inhomogeneities in the tissue is described mathematically by the scattering sources appearing on the right hand side of (2.2). Given exact knowledge of the spatial variations in κ and ρ throughout the propagation medium, the scattered wave field can therefore in theory be obtained as a part of the solution of this equation. In general, this solution is complicated and most easily obtained numerically. However, subject to particular boundary conditions and certain approximations, simple analytical solutions can also be found providing a great deal of insight. Insana and Brown [44] do this by first assuming a harmonic solution, i.e. one containing only one frequency component at the frequency $f = \omega/2\pi$, on the form $p(\mathbf{r}, t) = p_\omega(\mathbf{r})e^{-i\omega t}$. Inserting this into (2.2) results in the well-known and time-independent Helmholtz equation

$$\nabla^2 p_\omega + k^2 p_\omega = -s(\mathbf{r}), \tag{2.4}$$

where $k = \omega/c$ is the wave number and

$$s(\mathbf{r}) = k^2 \gamma_\kappa(\mathbf{r}) p_\omega(\mathbf{r}) - \nabla \cdot (\gamma_\rho(\mathbf{r}) \nabla p_\omega(\mathbf{r}))$$

is the scattering sources. More complex solutions containing several frequencies can then be found through linear superposition of such single-frequency solutions.

Now, (2.4) is a version of the more general Poisson equation, and a standard solution approach for such equations is by means of Green's functions, an introduction to which is given e.g. by McOwen [46]. Using this approach, assuming that all inhomogeneities in the medium are contained by a volume V in space with known properties $\kappa_\mathrm{e}(\mathbf{r})$ and $\rho_\mathrm{e}(\mathbf{r})$, (2.4) can be converted into an integral equation integrating over V. Insana and Brown [44] simplify the situation further by only considering the solution at observation points $\mathbf{r}$ in space far away from V, i.e. $\mathbf{r} \gg \mathbf{r_0}$ for all $\mathbf{r_0} \in V$. This is illustrated in figure 2.4 where the origin is placed within V, $\hat{\mathbf{i}}$ and $\hat{\mathbf{o}}$ are the unit vectors in the directions of the incident wave and the observation point respectively, and θ is the angle between these vectors referred to as the scattering angle. The resulting integral equation can thus be written [44]

$$p_\omega(\mathbf{r}) = p_\mathrm{i}(\mathbf{r}) + p_\mathrm{s}(\mathbf{r}),$$

where

$$p_\mathrm{s}(\mathbf{r}) \approx \frac{k^2 e^{ikr}}{4\pi r} \int_V \left[\gamma_\kappa(\mathbf{r_0}) p_\omega(\mathbf{r_0}) - i\gamma_\rho(\mathbf{r_0}) \left(\nabla_0 p_\omega(\mathbf{r_0}) \cdot \frac{\hat{\mathbf{o}}}{k}\right)\right] e^{-i\mathbf{k}_\mathrm{s} \cdot \mathbf{r_0}} \mathrm{d}\mathbf{r_0} \tag{2.5}$$

is the scattered wave, $r = |\mathbf{r}|$, ∇_0 denotes the gradient with respect to the integration variable $\mathbf{r_0}$, and $\mathbf{k}_\mathrm{s} = k\hat{\mathbf{o}}$ is the wave number in the direction of the observation point.

To solve this equation, the incident wave field p_i must be given. The wave field produced by an actual ultrasound transducer is in general a complicated one, and to produce a simple, analytical solution it is therefore common to consider only plane incident waves $p_\mathrm{i}(\mathbf{r}) = Pe^{i\mathbf{k}_\mathrm{i}\cdot\mathbf{r}}$, where $\mathbf{k}_\mathrm{i} = k\hat{\mathbf{i}}$. Another and more realistic assumption is that the scattering is weak compered to the incident wave, i.e. $p_\mathrm{s} \ll p_\mathrm{i}$. As mentioned, this is what is known as the Born approximation and implies that the part of the scattering caused by scattered waves from the surrounding medium, referred to as higher order scattering, is negligible compared to the first order scattering caused by the incident wave. This means that p_ω can be approximated by p_i in the computation of scattering, i.e. $p_\omega = p_\mathrm{i} + p_\mathrm{s} \approx p_\mathrm{i}$. Inserting this into (2.5) results in [44]

$$\begin{aligned} p_\mathrm{s}(\mathbf{r}) &\approx \frac{Pe^{ikr}}{r}\frac{k^2}{4\pi}\int_V \left[\gamma_\kappa(\mathbf{r_0}) + \gamma_\rho(\mathbf{r_0})\left(\hat{\mathbf{i}}\cdot\hat{\mathbf{o}}\right)\right] e^{-i\mathbf{K}\cdot\mathbf{r_0}}\mathrm{d}\mathbf{r_0} \\ &= P\frac{e^{ikr}}{r}\Phi(\mathbf{K}), \end{aligned} \tag{2.6}$$

where $\mathbf{K} = \mathbf{k}_\mathrm{s} - \mathbf{k}_\mathrm{i} = k(\hat{\mathbf{o}} - \hat{\mathbf{i}})$ is the scattering vector and Φ is the angle distribution factor. This expression can thus be used to calculate the pressure at points $\mathbf{r}$ on the surface of the ultrasound transducer caused by scattering sources relatively far away. Now, the scatterers in biological soft tissue are not contained in small volumes, and a plane incident wave would result in scattering signal from a very large area. However, ultrasound systems for B-mode imaging do not produce plane waves, but rather a sound pulse with a limited spatial extent, usually only a few millimeters in each direction. The backscattered signal received by the transducer in a certain time period originates from the small volume in space covered by this propagating pulse, and the integral in (2.6) can therefore be limited to this small volume.

The angle distribution factor Φ can also be expressed in terms of the scattering angle θ as

$$\Phi(\mathbf{K}) = \frac{k^2}{4\pi}\int_V \gamma(\mathbf{r_0},\theta)e^{-i\mathbf{K}\cdot\mathbf{r_0}}\mathrm{d}\mathbf{r_0} \tag{2.7}$$

with $\gamma(\mathbf{r_0},\theta) = \gamma_\kappa(\mathbf{r_0}) + \gamma_\rho(\mathbf{r_0})\cos\theta$. Now, an ordinary ultrasound imaging system uses the same transducer to transmit and receive the ultrasound waves, and for the received pressure this implies $\theta = \pi$, corresponding to 180°, and $\mathbf{K} = 2k$. It follows that

$$\gamma(\mathbf{r_0},\pi) = \frac{\Delta\kappa_\mathrm{e}(\mathbf{r_0})}{\kappa_0} - \frac{\Delta\rho_\mathrm{e}(\mathbf{r_0})}{\rho_\mathrm{e}(\mathbf{r_0})} \approx \frac{\Delta\kappa_\mathrm{e}(\mathbf{r_0})}{\kappa_0} - \frac{\Delta\rho_\mathrm{e}(\mathbf{r_0})}{\rho_0} = -\frac{2\Delta Z(\mathbf{r_0})}{Z_0}. \tag{2.8}$$

The contribution to Φ from a given point $\mathbf{r_0}$ in space is therefore approximately proportional to the relative variation in acoustic impedance $\Delta Z(\mathbf{r_0})/Z_0$ [44], and for a given volume V, the magnitude of Φ is proportional to the average of this variation.

To find the intensity I_s of the backscattered wave reaching the ultrasound transducer, it is convenient to define the *backscatter coefficient* σ_b. This can be done by considering an incident wave with intensity I_i reaching a volume

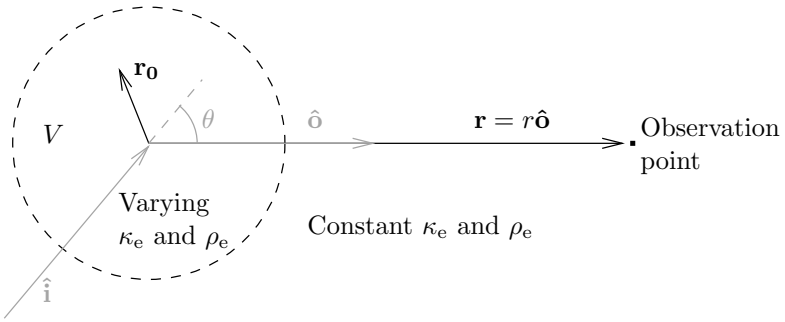

Figure 2.4: Schematic description of the scattering situation. All inhomogeneities are assumed to be contained by the volume V, and κ_e and ρ_e are thus constant outside of V. Moreover, the observation point is assumed to be far away from V, i.e. $\mathbf{r} \gg \mathbf{r_0}$ for all $\mathbf{r_0} \in V$. $\hat{\mathbf{i}}$ and $\hat{\mathbf{o}}$ are unit vectors in the directions of the incident wave and the observation point respectively.

V containing inhomogeneities. The wave is scattered in all directions, and the scattered power per unit solid angle divided by I_i is referred to as the *differential scattering cross section* denoted by σ_{ds} . It can be shown that $\sigma_{ds} = |\Phi(\mathbf{K})|^2$ [44]. The backscatter coefficient is then defined as differential scattering cross section per unit volume for scattering angle $\theta = \pi$, i.e.

$$\sigma_b = \frac{\sigma_{ds}|_{\theta=\pi}}{V} = \frac{|\Phi(2k)|^2}{V}. \tag{2.9}$$

Typical values for some soft tissues can be seen in table 2.2 [9]. Knowing σ_b, the scattered power Π reaching the ultrasound transducer can now be found as $\Pi = I_i V \sigma_b \Omega$, where Ω is the solid angle spanning the surface of the transducer. Assuming that the distance r to the scattering sources is large compared to the area A of the transducer, Ω can be approximated by A/r^2. The intensity received by the transducer is then given by

$$I_s = \frac{\Pi}{A} = \frac{I_i V \sigma_b \Omega}{A} = \frac{I_i V}{A} \frac{|\Phi(2k)|^2}{V} \frac{A}{r^2} = \frac{I_i}{r^2} |\Phi(2k)|^2 ,$$

and since Φ is shown to be approcimately proportional to $\Delta Z(\mathbf{r_0})/Z_0$, this can be written

$$\frac{I_s}{I_i} = \frac{\zeta}{r^2} \left| \frac{\Delta Z(\mathbf{r_0})}{Z_0} \right|^2 , \tag{2.10}$$

where ζ is a proportionality constant and $\mathbf{r_0}$ is a typical point within the small volume V.

Absorption

As mentioned, the model developed so far does not account for absorption losses. It is possible to derive a wave equation from first principles accounting for such effects [47], but the resulting expressions describing the wave field are complicated. However, by assuming that the acoustic absorption of the wave is uniform

Table 2.2: Typical values for the backscatter coefficient σ_b at 5 MHz in some soft tissues [9].

Material	Backscatter coefficient σ_b [$\mathrm{cm}^{-1}\mathrm{sr}^{-1}$]
Blood	$1.4 \cdot 10^{-5}$
Myocardium	$7.0 \cdot 10^{-4}$
Liver	$2.0 \cdot 10^{-3}$
Kidney	$1.1 \cdot 10^{-3}$

throughout the medium, it can be included in the solution of (2.2) by means of a complex wave number $k = \omega/c + i\alpha_p$, where α_p is a characteristic absorption coefficient [44]. Inserting this into the expression for a plane wave $p(\mathbf{r}) = Pe^{i\mathbf{k}_\mathrm{i} \cdot \mathbf{r}}$, it is easy to see that the imaginary part of k causes an attenuation of the wave with a factor $e^{-\alpha_p r}$. Since the intensity of the wave is proportional to the square of the pressure amplitude, it follows directly that the intensity $I(\mathbf{r})$ of the wave is attenuated by a factor $e^{-\alpha_I r}$, where $\alpha_I = 2\alpha_p$ [7]. In general, both α_p and α_I are functions of frequency $f = \omega/2\pi$. A common rule of thumb is that the absorption in human tissue is approximately 0.5 dB/cmMHz, and this implies an absorption coefficient

$$\alpha_I(f) = 115 \cdot 10^{-9} f. \tag{2.11}$$

Display

The attenuation of ultrasound waves caused by its interaction with the propagation medium increases with travelled distance. The intensity of the received signal thus drops as a function of depth, causing similar targets to appear different depending on distance from the transducer. To compensate for this, ultrasound scanners apply a depth-dependent amplification referred to as time gain compensation (TGC). This makes it possible to compare objects at different depths in the resulting image.

Now, the range of intensities which a modern ultrasound scanner can detect is enormous. The ratio of the strongest signal from reflectors close to the transducer to the weakest signal from small scatterers deep into the medium can be as large as 120 dB [6]. As the TGC amplifies the weakest signals, this ratio is typically reduced to about 60 dB, but this is still a much larger than what can be handled by the monitors used in ultrasound scanners. To prepare the signal for display, a logarithmic compression of the signal is therefore performed. This attenuates the strongest signal components and amplifies the weak ones, additionally reducing the span of intensities to 20 to 30 dB.

Image quality

The quality of the ultrasound images basically depends on spatial resolution, which is the ability to resolve closely spaced point targets, and contrast resolution, which is the ability to detect small variations in the intensity from closely spaced targets [7]. The most important factors determining the spatial resolution are the length of the ultrasound pulse and the width and height of the

ultrasound beam [7]. All are limited by the capabilities of the ultrasound system in terms of such parameters as bandwidth, transmission frequency, aperture width and number of transducer elements. The spatial resolution is also affected by inhomogeneities in the propagation medium causing small variations in the propagation speed of the sound waves. These variations bring about aberrations of the wave front and refractions of the sound beam, both resulting in defocusing of the sound beam and geometric distortions of the final ultrasound image. They also introduce errors in the depth ranging performed by the ultrasound scanner as this erroneously assumes that the speed of sound is constant.

Contrast resolution, on the other hand, is primarily dependent on the noise level of the system [7]. All electronic equipment generate a certain amount of electronic noise, which is random signal unrelated to the input [48], and the ability to detect small differences in intensity is fundamentally limited by the level of this noise, often referred to as the noise floor of the system. Since this noise appears in the electronic part of the system, it is not attenuated with depth like the acoustic signal. The signal-to-noise ratio thus decreases with depth.

However, when it comes to ultrasound imaging, the main limitation on the contrast resolution is actual acoustic signals which do not correspond to any physical structures in the imaged medium [7]. These signals, referred to as signal generated noise, create artifacts in the ultrasound images obscuring the signal from real structures in the medium. There are several acoustic phenomenons which contribute to this. A typical example is speckle pattern which is a characteristic feature in ultrasound images of biological soft tissues. Such tissues contain a lot of small, subresolution structures, and scattered ultrasound components from these interact with each other creating an interference pattern. This is what is known as speckle [43].

Another example is reverberations. As ultrasound waves reflected by interfaces in the propagation medium travel back towards the transducer, they may encounter new interfaces. A part of the wave is then reflected a second time, thus creating a new incident wave which may again be reflected by new surfaces. As the multiply reflected parts of these waves reach the transducer, they will arrive together with signal from deeper within the medium, thus creating artifacts at other depths than the original interface. These multiple reflections are known as reverberations [45]. A common source of such artifacts are strongly reflecting interfaces close to the transducer [6]. Since the transducer itself is a strong reflector, waves may start bouncing back and forth between this and the interface. Each time these waves reach the transducer, they will have travelled the same distance, i.e. out to the reflector and back again, and the result is that the interface is duplicated at evenly spaced depths throughout the ultrasound image.

The contrast resolution is also affected by limitations in the beam forming capabilities of the ultrasound transducer [45]. The achieved ultrasound beam will in general not be a single, narrow beam, but rather consist of a strong main lobe in the forward direction accompanied by several weaker side lobes. As a consequence, the scattered signal arriving at the transducer consists of components not only from the target area interrogated by the main lobe, but also from certain areas around this. These extra components appear in the image as if they also originated from the target area, thus producing artifacts deteriorating the contrast resolution.

When the imaged object is moving, time resolution also becomes critical

to the image quality. In principal, this is fundamentally limited by the speed of sound in the medium as each pulse must reach the target and return to the transducer before a new pulse can be sent. However, techniques exist which allow an increase in the frame rate beyond this limit, mainly by parallel processing of several receive beams for each transmitted ultrasound pulse [49].

Chapter 3

Materials and Methods

The simulation method developed in the USSim project uses the interpolation approach described in section 2.1 to produce artificial ultrasound images in real time based on the information in a three-dimensional CT data set. Extracting a slice from this data set, the method computes both shadows, specular reflections and speckle patterns typical of ultrasound images and adds these artifacts to the CT slice. However, these computations are mainly based on qualitative information in the extracted CT image such as the location of visible edges or particularly light or dark areas, thus neglecting both the quantitative information provided by CT numbers and physical models for wave propagation. In order to explore the potential in using such resources, a new simulation method was therefore made as a part of this master's project. It was based on the platform of the previous method and aimed at improving the realism of the simulated images while still retaining the real time performance. The new method was evaluated using an experimental setup facilitating a comparison of the simulated images with corresponding true ultrasound images. This chapter provides a description of both the simulation method and the evaluation setup.

3.1 Simulation method

The simulation method was implemented in the numerical computing programme MATLAB from The MathWorks (Natick, MA, USA), and its purpose was to produce simulated ultrasound images of a given object based on the information in a CT scan of this object. The method was organized in three main modules:

CT data processing, which imports and prepares the provided CT data and extracts the appropriate two-dimensional slice from them.

Simulation, which computes artificial ultrasound artifacts from the given CT slice and produces an artificial ultrasound image.

Display, which converts the simulated image according to the given scan sector geometry, what is known as scan convertion, and displays the final image on the computer screen.

These modules corresponded to those implemented in the the previously developed prototype, and whereas the first and the last module were kept unaltered,

the simulation module was changed in its entirety. A schematic drawing of the simulation method can be seen in figure 3.1.

The CT data set which was used in the development of this method was taken from a multi-modality imaging phantom (CIRS, Norfolk, VA, USA) [50]. It consisted of 33 slices with an effective slice thickness of 4 mm and a resolution of 0.6 mm × 0.6 mm. These CT data were initially read into a three-dimensional MATLAB matrix, and a two-dimensional ultrasound scan sector consisting of 128 scan lines was defined within the coordinates of this matrix. Each scan line represents an ultrasound beam and points in the propagation direction of the beam. The size and geometry together with position and orientation of the scan sector were given as input to the method, and based on this information the CT numbers h at 500 evenly spaced points along each scan line were found through linear interpolation. Each sample was taken to represent a resolution volume, i.e. the small volume within the imaged medium contributing to one sample of the ultrasound signal. Assuming a sector depth of 20 cm, this implies

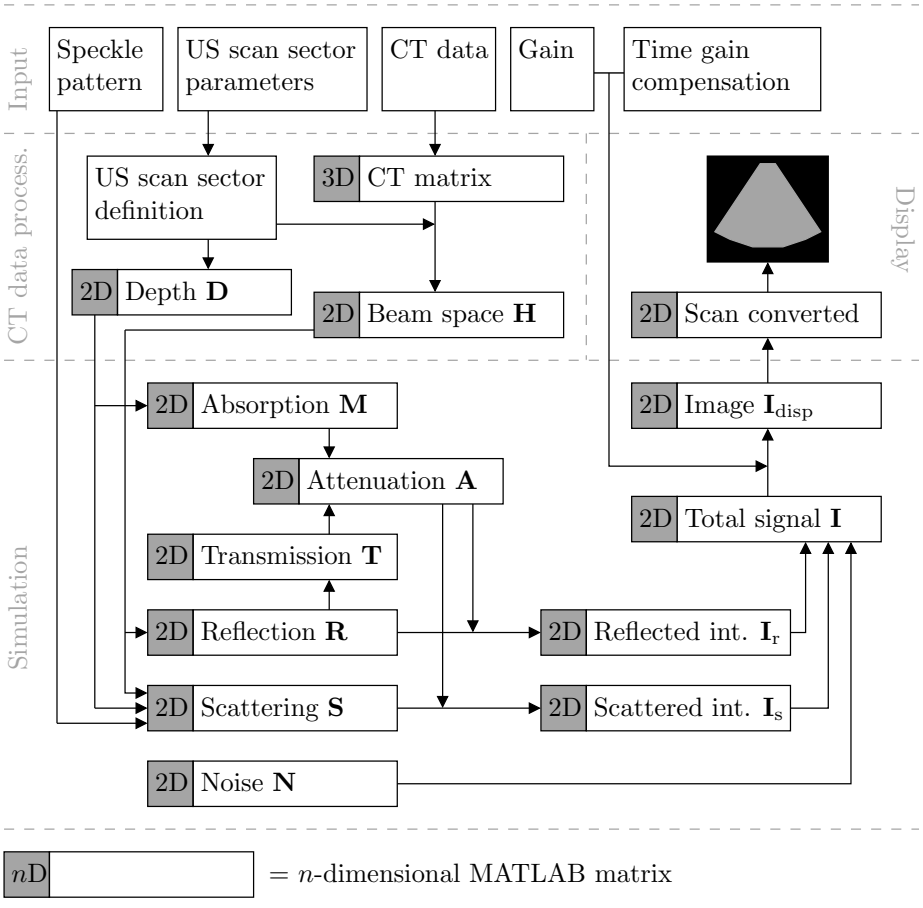

Figure 3.1: Schematic drawing showing the elements and data flow of the developed simulation method. The different procedures and computations are represented by arrows. The boldfaced letters are the mathematical symbols representing each matrix.

an axial resolution of about 0.4 mm, which is reasonable for B-mode imaging [6]. The obtained CT numbers were then stored in a two-dimensional matrix **H** with each column representing a scan line. This is referred to as a beam space representation of the data and is illustrated in figure 3.2.

Reflection, transmission and attenuation

Having processed the CT data, the first goal of the simulation module was to compute the specular reflections visible in ultrasound images. As described in section 2.3, such reflections are due to macroscopic variations in acoustic properties. Knowing these properties in terms of the acoustic impedance Z, the appropriate reflection and transmission coefficients can be computed. To obtain Z, defined as $Z = \rho c$, for the given scan sector, the density ρ was first estimated using the CT numbers in **H** together with the relationship given in (2.1). Since this relationship only is valid for certain groups of CT numbers not covering the entire range, the tissue groups given in table 2.1 first had to be expanded. Also, a group for particularly low CT numbers, assumed to be air, was added. This group was assigned the density $\rho = 1.2\ \mathrm{kg/m^3}$ [6]. The resulting tissue groups and density estimates are shown in table 3.1.

In order to derive the acoustic impedance Z from these computed densities, each of the defined tissue groups was assigned a representative value for the speed of sound c. This is an acceptable approximation for air and soft tissues where the variations in c are small [7]. In skeletal tissues, the variations are larger, but since these tissues reflect almost all sound anyway, the resulting error in Z has no impact on the final simulations. The values which were used are shown in table 3.1 [7]. Knowing the speed of sound and the density for each of the elements in the beam space matrix, the acoustic impedance was found and stored in the impedance matrix **Z**.

Now, as the imagined ultrasound pulse reaches a point along a scan line, it is reflected and transmitted according to the reflection and transmission coefficients at that point. These coefficients depend on the impedance Z_1 of the medium the pulse arrives from and the impedance Z_2 of the medium it enters. For each element in the beam space representation, these two quantities were therefore estimated as a weighted average of the impedances of the 10 previous elements and the 10 next elements respectively. The number of elements was chosen as low as possible while still producing sufficient attenuation at strong reflectors such as bone. Inserting the estimates into the formulas in (2.3), re-

Table 3.1: Tissue groups and corresponding formulas used to calculate densities ρ based on CT numbers h. Typical values for the speed of sound c, taken from Angelsen [7], are also given.

Tissue group	CT Numbers h	Density estimate $\rho(h)$ [kg/m^3]	Speed of sound c [m/s]
Air	$h < -900$	1.2	330
Soft tissues	$-900 \leqslant h < 20$	$1017 + 0.592h$	1440
Dense soft tissues	$20 \leqslant h < 200$	$1018 + 0.893h$	1540
Skeletal tissues	$h \geqslant 200$	$1003 + 1.169h$	4100

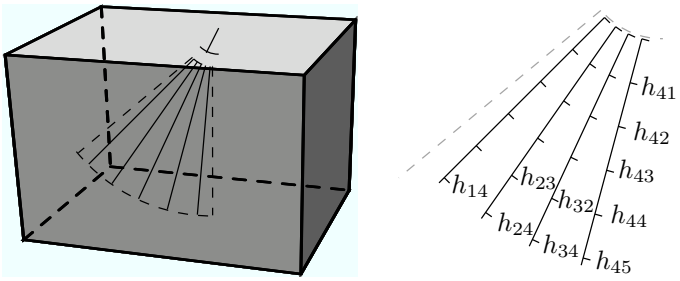

(a) **(b)**

$$\mathbf{H} = \begin{bmatrix} h_{11} & h_{12} & \dots \\ h_{21} & h_{22} & \dots \\ \vdots & \vdots & \ddots \end{bmatrix}$$

(c)

Figure 3.2: Three-dimensional CT volume and scan sector consisting of scan lines. Each column of the beam space matrix $\mathbf{H}$ in figure (c) hold the CT numbers h of one scan line in the scan sector.

flection and transmission coefficients of the wave intensity were computed for all elements except for the 10 first and the 10 last in each scan line. Here, at the edges, information about either Z_1 or Z_2 was unavailable and, assuming no reflection, R_I was set to 0 and T_I was set to 1. The results were stored in a reflection matrix $\mathbf{R}$ and a transmission matrix $\mathbf{T}$. However, $\mathbf{R}$ only contains information about the fraction of the wave which is reflected at each point. In order for the reflection to appear in the ultrasound image, the point must be part of an interface which is perpendicular to the propagation direction of the beams, i.e. parallel to the rows in the beam space representation. To imitate this effect, a smoothing filter was applied to each of the rows of $\mathbf{R}$. In this way, high reflection coefficients appearing side by side on a row, thus representing a perpendicular interface, were strengthened, while single high values of $\mathbf{R}$ were attenuated.

The specular reflections cause an attenuation of the transmitted ultrasound wave. In this context, the transmission coefficients can be seen as attenuation factors describing the decrease in wave intensity upon passing a given interface. To find the total attenuation of a wave reaching a point in beam space, say the ith point in the jth scan line, all transmission coefficients preceding the point along the scan line, i.e. $T^{1,j}$ to $T^{i-1,j}$, should be multiplied with each other. Since the coefficients are symmetric, this is also the attenuation experienced by reflected waves travelling from the point towards the transducer. However, reflection is not the only process contributing to the attenuation of the sound waves. As described in section 2.3, acoustic absorption also leads to attenuation, and by assuming that this absorption is uniform throughout the medium, it can be described by an exponential attenuation factor $e^{-\alpha_I r}$, where α_I is a characteristic absorption coefficient and r is the travelled distance.

For the points in the beam space representation, information about the distance r to the ultrasound transducer was given as input to the simulation method

as a part of the scan sector definition. Combining this information with the estimate for α_I given in (2.11), an absorption attenuation factor for each point in beam space was computed and stored in an absorption matrix $\mathbf{M}$. By also taking into account the previously computed transmission coefficients, a total attenuation matrix $\mathbf{A}$ was found. Its elements, given as $A^{i,j} = T^{1,j} \cdots T^{i-1,j} M^{i,j}$, thus describe the total intensity attenuation of a wave travelling from the transducer to the point (i, j) or from the point to the transducer. Given a transmitted incident intensity I_i, the intensity of the specular reflection from the point (i, j) was now found as

$$I_\mathrm{r}^{i,j} = I_\mathrm{i} A^{i,j} R^{i,j} A^{i,j}, \tag{3.1}$$

and, letting $\circ$ denote elementwise multiplication, this computation could be performed collectively for all points in beam space as

$$\mathbf{I}_\mathrm{r} = I_\mathrm{i} \mathbf{A} \circ \mathbf{R} \circ \mathbf{A}.$$

Due to small impedance variations, the reflection matrix $\mathbf{R}$ is nonzeoro almost everywhere, and the resulting intensity matrix $\mathbf{I}_\mathrm{r}$ therefore contains a contribution from nearly every point in beam space. However, specular reflections only occur at macroscopic tissue interfaces, and the small contributions from the rest of the points in beam space do not correspond to any physical phenomenon. Every intensity value below a certain threshold was therefore set to 0. Based on inspection of the simulated reflections, this threshold was set to about 0.5% of the intensity of the strongest reflections.

Reverberations

Now, ultrasound transducers are relatively hard compared to soft tissue, and as the specular reflections from the tissue reach this interface, they are therefore reflected again. If these secondary reflections are strong, they may cause artifacts known as reverberations in the ultrasound images. It is a very complex task to compute all the possible reverberations which may occur. However, a common source of such artifacts is waves bouncing back and forth between one particularly strong reflector and the transducer, and these reverberations are more easily obtained. In order to do this, the reflection coefficient at the transducer surface was very roughly approximated by assuming total reflection. Given a strong reflector at the point (i, j) in beam space, this implies that the reflection arriving from this point is completely reflected by the transducer, thus crating a new wave with incident intensity $I_\mathrm{r}^{i,j}$. As this wave reaches back to the reflector at (i, j), it will cause a second reflection, and as in (3.1) the intensity of this reflection is given by $I_{\mathrm{r},2}^{i,j} = I_\mathrm{r}^{i,j} A^{i,j} R^{i,j} A^{i,j}$. Similarly, the kth reflection created in this way has an intensity given by $I_{\mathrm{r},k}^{i,j} = I_{\mathrm{r},k-1}^{i,j} A^{i,j} R^{i,j} A^{i,j}$. Using this, the multiple reflections for all points in beam space were computed as

$$\mathbf{I}_{\mathrm{r},\mathbf{k}} = \mathbf{I}_{\mathrm{r},\mathbf{k-1}} \circ \mathbf{A} \circ \mathbf{R} \circ \mathbf{A}, \qquad \text{for } k = 2, 3, 4, 5.$$

As for the original reflections, it was assumed that intensity values below a given threshold did not correspond to actual reflections, and these values were therefore set to zero.

Since the kth reflection from the reflector at point (i, j) has used k times as long time to reach the transducer as the first reflection, an ultrasound scanner

will interpret this reflection as coming from a point k times as deep within the body, i.e. the point (ki, j). In order to display the computed reverberations correctly, the matrices $\mathbf{I}_{\mathrm{r},\mathbf{k}}$ were therefore all stretched with a factor k by means of linear interpolation, thus placing the reflections at the correct point in beam space. Since signal falling outside of the ultrasound sector could be ignored, the matrices were finally truncated to the size of $\mathbf{I}_{\mathrm{r}}$ before they all were added together. The result was that $\mathbf{I}_{\mathrm{r}}$ now contained both the original reflections and all computed reverberations.

Scattering

Having determined the specular reflections and reverberations, the next goal was to compute the signal caused by the scattering of ultrasound in soft tissue. According to (2.10), the relationship between incident intensity I_{i} and scattered intensity I_{s} measured at the transducer surface depends upon three factors: the relative variations in impedance $\Delta Z/Z_0$ within the scattering volume V, the distance r to this scatterer and a proportionality constant ζ. In this context, V is the small volume within the imaged medium contributing to one sample of the received ultrasound signal, and it thus corresponds to the resolution volume of the system. Since each point in beam space was assumed to represent one such volume, the impedance values in $\mathbf{Z}$ could be used directly. The local average Z_0 at a given point was then estimated as the median of all impedance values in a 20×20 neighbourhood around this point. The resulting values were stored in a median matrix $\mathbf{Z_0}$. As previously mentioned, the distance r to each of the points in beam space was given as input to the simulation method as a part of the scan sector definition, and these were stored in the beam space matrix $\mathbf{D}$. The only quantity left was thus the constant ζ which arises from the proportional relationship between the angle distribution factor Φ and $\Delta Z/Z_0$. As seen in (2.9), Φ can be expressed in terms of the scattering volume V and the backscatter coefficient σ_{b}. Since V corresponds to the resolution volume of the ultrasound system, it is typically around $0.02\ \mathrm{cm}^3$ [6]. Common values for σ_{b} are given in table 2.2, and for soft tissue these are all around $1 \cdot 10^{-3}\ \mathrm{cm}^{-1}\mathrm{sr}^{-1}$. Since both Z and Z_0 had already been computed, an average value for $|\Delta Z/Z_0|^2$ could also be found, and inserting these estimates into (2.9) resulted in a typical value of about $0.4\ \mathrm{cm}^2$ for the constant ζ.

To facilitate the computation of the scattered intensity, a new scattering coefficient was now defined as $S_I = I_{\mathrm{s}}/I_{\mathrm{i}}$, analogous to the reflection coefficient R_I. S_I could then be found for each element in beam space by combining the computed values for Z and r with the estimates for Z_0 and ζ according to (2.10). As for the reflection coefficients, this computation was performed collectively for all elements as

$$\mathbf{S} = \zeta \mathbf{D}^{-2} \circ ((\mathbf{Z} - \mathbf{Z_0}) \circ \mathbf{Z_0}^{-1})^2,$$

where both the multiplications and the exponentiations are taken to be elementwise.

Now, since these computations only consider one element, and thus only one scatterer, at a time they do not produce any speckle pattern. This pattern is a result of the interaction between scattered components from many small, subresolution structures and is a characteristic feature of ultrasound images. To incorporate this in the model, a beam space representation of a typical speckle

pattern was obtained in an offline process using the ultrasound simulation program Field II made by Jørgen A. Jensen [24, 25].This pattern was then merged with the matrix $\mathbf{S}$ through elementwise multiplication. Taking incident intensity and attenuation into account, the intensity of the scattered wave was finally computed as

$$\mathbf{I}_\mathrm{s} = I_\mathrm{i}\mathbf{A} \circ \mathbf{S} \circ \mathbf{A}. \tag{3.2}$$

Electronic noise, TGC and compression

The last contribution to the ultrasound signal, was electronic noise. Assuming a noise floor N, this was modeled as a noise matrix $\mathbf{N}$ where each element was given a random value between 0 and N. Combining this with the reflected and scattered components, the total intensity of the ultrasound signal was given as $\mathbf{I} = \mathbf{I}_\mathrm{r} + \mathbf{I}_\mathrm{s} + \mathbf{N}$. A typical example of a beam space representation of each of the simulated signal components is shown in figure 3.3. Also, to counteract the effect of the signal attenuation, a time gain compensation (TGC) was implemented. The values of this added gain at eight evenly spaced depths were given as input to the simulation method. The corresponding values for all other depths were then determined by linear interpolation before multiplying each element of the intensity matrix $\mathbf{I}$ with the appropriate gain factor producing the intensity matrix $\mathbf{I}_\mathrm{TGC}$. In order to prepare the simulated ultrasound signal for display, this signal was multiplied by a global gain factor Γ and logarithmically compressed so that the final signal was given by

$$\mathbf{I}_\mathrm{disp} = 10\log_{10}\left(\frac{\Gamma\mathbf{I}_\mathrm{TGC}}{I_\mathrm{i}}\right).$$

Passing the resulting beam space matrix $\mathbf{I}_\mathrm{disp}$ on to the display module, an ultrasound image was then drawn according to the geometry of the scan sector. Since the coordinates of the data points stored in $\mathbf{I}_\mathrm{disp}$ in general did not correspond to the pixels of the new image, the intensities of these pixels were obtained through linear interpolation. This conversion of the beam space representation into a proper image is known as scan conversion, and this concluded the simulation method.

3.2 Experimental setup for evaluation

In order to evaluate the presented simulation method, both during the development process and upon completion, an experimental setup was adopted. The setup was developed as a part of the project work performed by the candidate in the fall of 2007 [13], and it was specifically designed for the evaluation of real time ultrasound simulators. Its main function is to produce true ultrasound images corresponding to the artificial ones made by the simulator, thus allowing a direct and intuitive evaluation through the comparison of these images.

The setup, shown in figure 3.4, incorporates a multi-modality imaging phantom (CIRS, Norfolk, VA, USA) and a System FiVe ultrasound scanner (GE Vingmed, Horten, Norway) fitted with a 3.5 MHz CLA probe. In addition, the Polaris Spectra optical measurement system (NDI, Waterloo, Canada) is used to track the positions and orientations of the probe and the phantom. Prerecorded CT images of the phantom are given as input to the simulator in question,

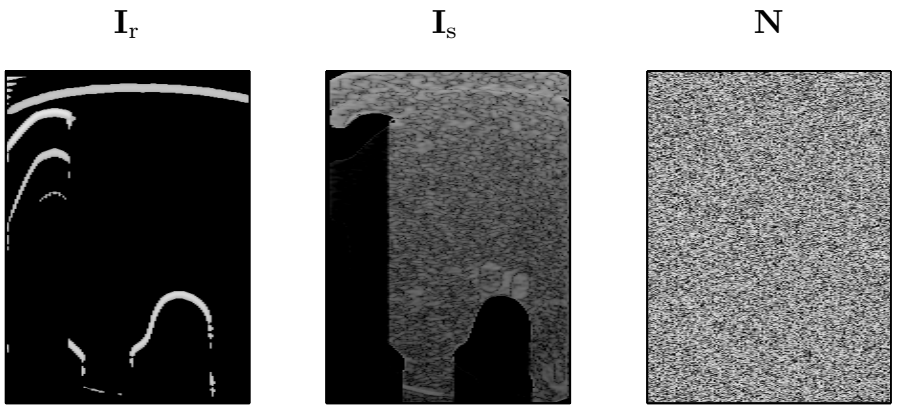

Figure 3.3: Beam space representations of typical simulated signal components: specular reflections $\mathbf{I}_r$, scattered signal $\mathbf{I}_s$ and electronic noise $\mathbf{N}$.

and the relationship between the physical frame of reference and the frame of reference of the CT images is found through a registration procedure. This is performed using the navigation software CustusX (SINTEF, Trondheim, Norway). Using this registration together with a calibration relating the position of the ultrasound probe to that of the ultrasound scan sector, the position of the scan sector can be passed to the simulator. Based on this information and the information in the CT images, the simulator can then produce simulated images corresponding to the real ultrasound images produced by the ultrasound scanner. The image acquisition can be performed in two different ways:

Real time acquisition where the simulator is continuously provided with position data during the ultrasound scan. The images can thus be displayed on the screens of the ultrasound scanner and the simulator simultaneously allowing real time comparison.

Offline acquisition where the ultrasound images are recorded together with the corresponding position data using Custus X. The position data are subsequently transferred to the simulator which performs a simulation and prints the corresponding images to a file. Corresponding real and simulated ultrasound images are then available for offline comparison.

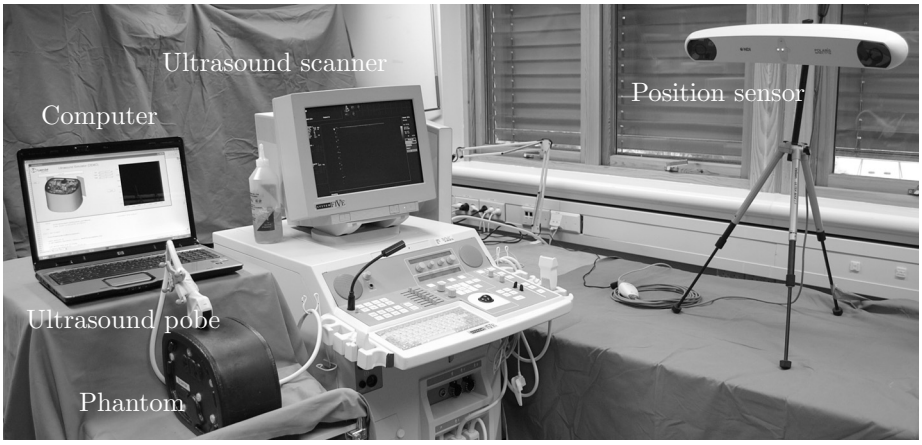

Figure 3.4: Laboratory setup for evaluation of ultrasound simulators. The setup incorporates a multi-modality imaging phantom (CIRS, Norfolk, VA, USA), a System FiVe ultrasound scanner (GE Vingmed, Horten, Norway), the Polaris Spectra optical measurement system (NDI, Waterloo, Canada) and a laptop computer running the given ultrasound simulator.

Chapter 4

Results

In this master's project, a simulation method has been developed and implemented in the numerical computing programme MATLAB. The method, which follows the interpolation approach described in section 2.1, is based on the platform of a previously made prototype simulator, and it is capable of producing artificial ultrasound images based on the information in a CT data set. The current implementation uses about one second to produce an image.

4.1 General comparison of images

In figures 4.1(a)–(b), two examples of simulated images produced by the new simulation method are presented. These simulations are based on CT data recorded from a multi-modality imaging phantom imitating the anatomy of a human abdomen. The images were produced with a signal-to-noise ratio I_i/N of 85 dB, where I_i is the intensity of the transmitted wave and N is the level of the noise floor. Figures 4.1(c)–(d) show simulations produced by the previously implemented prototype based on the same CT data. To facilitate an assessment of the realism of the simulations, true ultrasound images corresponding to the simulated ones are also given in figures 4.1(e)–(f). These images were acquired using the experimental setup described in section 3.2.

The reflections seen in the simulated images correspond well to those seen in the true ultrasound images. However, the weak reflection at the top of both ultrasound images is properly reproduced only by the new simulation method. The shape of this reflection, on the other hand, is not correct in either of the simulations. The simulated shadows are correctly placed, but they do in general have much sharper edges than those in the true ultrasound images. Almost the same applies to the reverberations produced by the new simulation method as seen within the shadow to the left in figure 4.1(b): they correspond well to those seen in the true ultrasound images, but they are far too strong.

Soft tissue components are not well reproduced in figures 4.1(a)–(b). The texture is somewhat finer than what is seen in figures 4.1(c)–(d), and this seems to correspond well to what is seen in the true ultrasound images. However, the white, disk-shaped structures seen at the bottom of the images in figures 4.1(c)–(f) are only faintly visible in the new simulations. Finally, the true ultrasound images are also more noisy than the simulated ones. This is particularly pro-

nounced in the right hand part of figure 4.1(e): both reflections and soft tissue structures clearly seen in the simulated images are here completely obscured by noise.

4.2 Attenuation and TGC

The simulated ultrasound signal experiences an attenuation due to reflection, absorption and geometric spread of the scattered signal. However, as in true ultrasound imaging this is counteracted by the time gain compensation (TGC), and attenuation effects are therefore normally not seen in the simulations. Figure 4.2(a) shows a simulated image with no TGC, illustrating the effect of the implemented attenuation factors. The same simulation with TGC is seen in figure 4.2(b). Here, the intensity of the soft tissue components is even throughout the image, but at the same time the electronic noise is amplified, particularly in the lower part of the image. This corresponds to what is seen in the true ultrasound image in figure 4.2(e) where the electronic noise, most visible in the shadow on the left, is strongest in the lower part of the image.

4.3 Electronic noise

Electronic noise is present in all ultrasound systems, but the level of this noise varies a lot. In figures 4.2(c) and (d), two images are shown with a high and a low noise level respectively. The noise obscures most of the actual ultrasound signal in the first image, whereas it is hardly visible in the second one. The image in figure 4.2(b) has a medium noise level quite close to the corresponding true ultrasound image in figure 4.2(e).

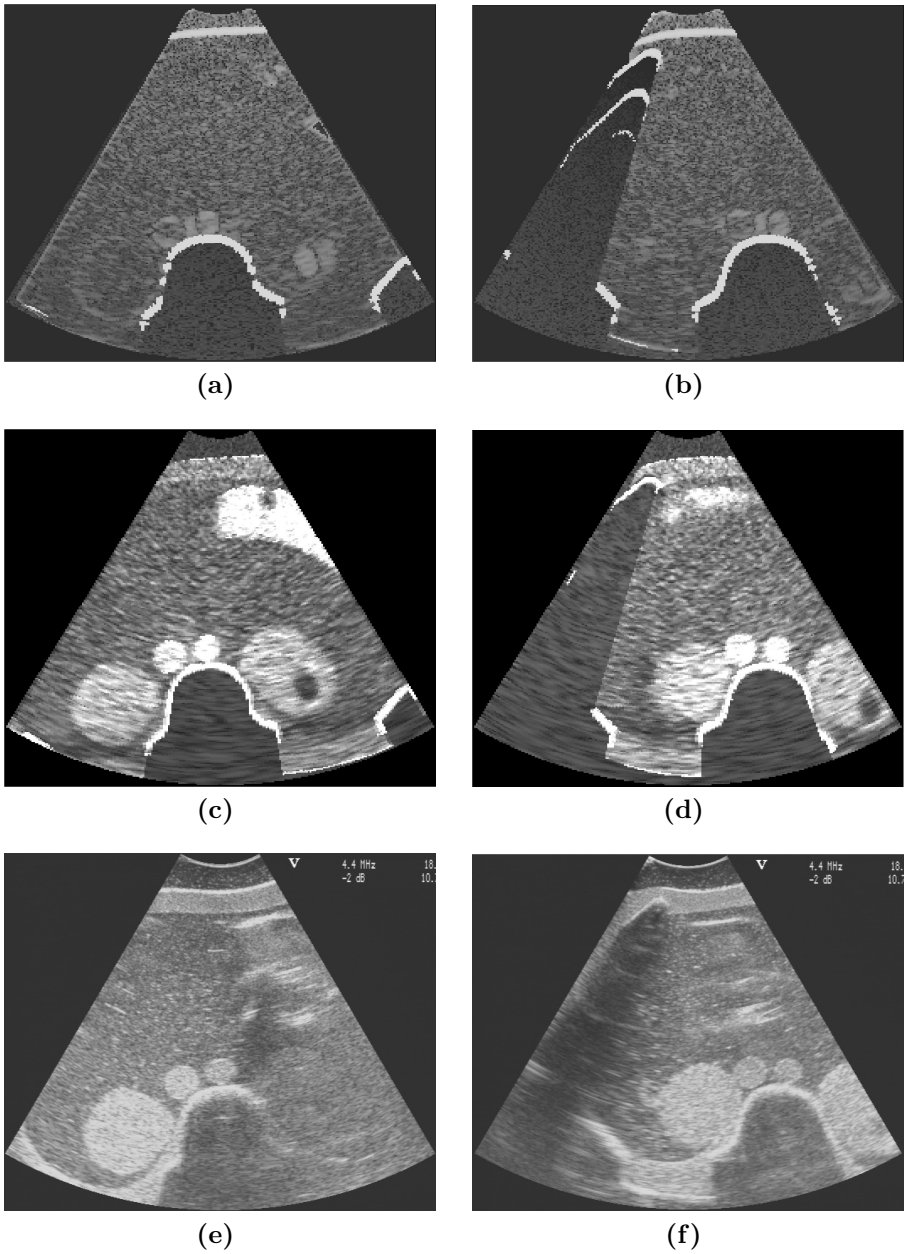

Figure 4.1: (a)–(b) Simulated ultrasound images produced by the simulation method presented in section 3.1 based on CT images from a multi-modality imaging phantom, and (c)–(d) simulated images produced by a previously developed simulation method based on the same CT data. Corresponding true ultrasound images, acquired using the experimental setup described in section 3.2, are shown in figures (e)–(f).

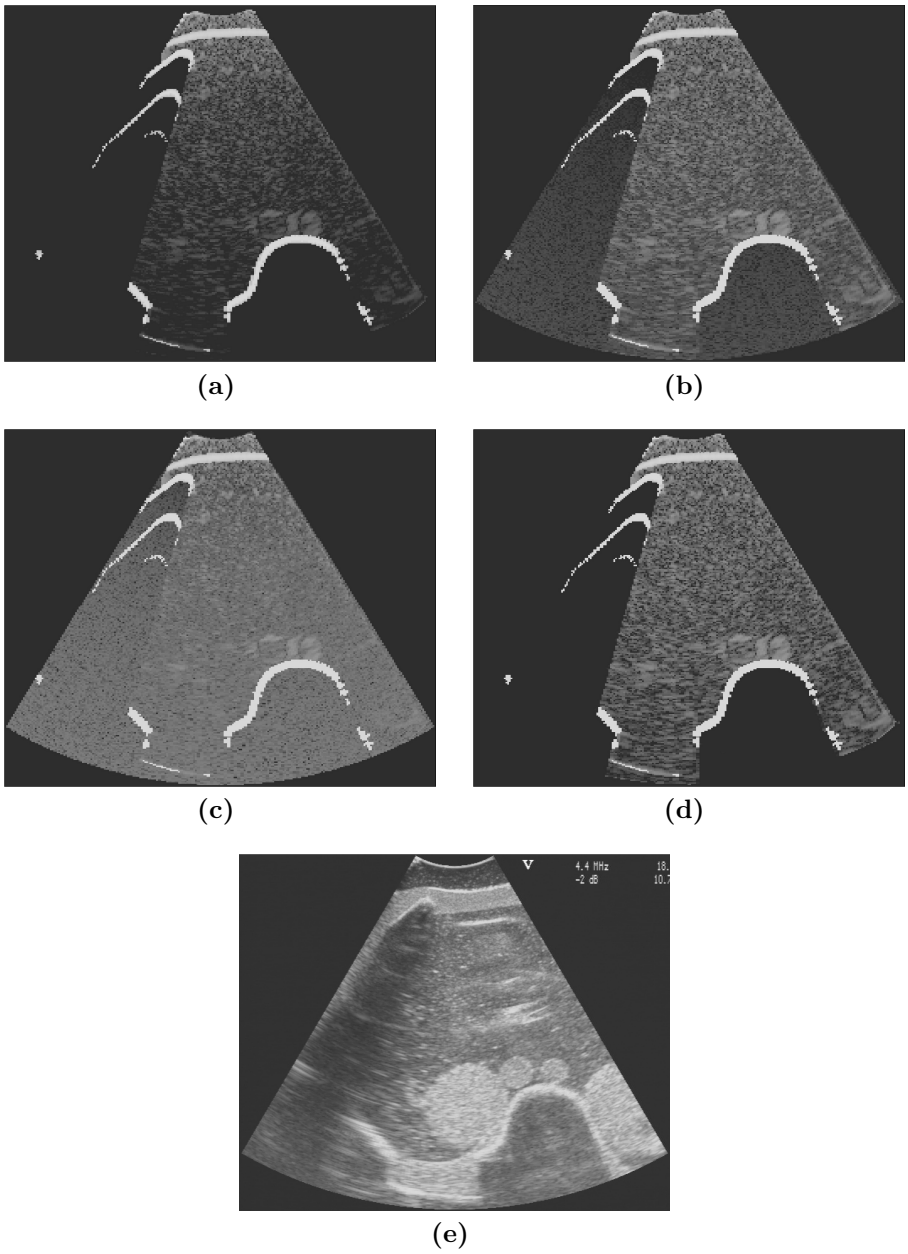

Figure 4.2: (a) Simulated ultrasound image with no time gain compensation (TGC) and (b) the same image with normal TGC. Both images have a medium noise level with a signal-to-noise ratio I_{i}/N of 85 dB. Figures (c) and (d) show the same images with high and low noise level respectively. The signal-to-noise ratios are (c) 70 dB and (c) 100 dB. The corresponding true ultrasound image is shown in figure (e).

Chapter 5

Discussion

The goal of the presented simulation method was to compute the appearance of features typical of ultrasound images based on the quantitative information available in CT images. This chapter first deals with the attempt at extracting information about acoustic properties, in terms of acoustic impedance, from the CT data. It then discusses the different effects included in the simulations in light of the results presented in chapter 4. Finally, since the simulation method is intended used in a training simulator based on CT data collected in a clinical setting, the performance of the presented method relative to this application is treated.

5.1 Estimation of acoustic impedance

The estimates of acoustic impedance Z performed in the first part of the simulation method are fundamental as several of the following computations are based on them. The linear relationship between CT numbers h and mass density ρ is well known [6], and the correlations found by Schneider et al. [41] should therefore be reasonably accurate within the range of CT numbers considered in their study. This includes most kinds of human tissue except for lung tissue. Applying the same relationships outside of this range, as is done in these estimates, is not as straight forward. However, since the simulation method is meant to be applied to CT data from human beings, the processed CT numbers will in most cases fall within the valid range, and the resulting error is therefore relatively small.

The impedance Z is dependent on both mass density ρ and compressibility κ, and since the CT images provide no information about the latter, an assumption of constant speed of sound c is applied, implying a linear relationship between ρ and κ^{-1}. The variations in c are indeed reported to be very small for biological soft tissues [7], and in many applications this approximation is therefore good. This is e.g. the case when it comes to the computation of reflections since these mainly occur at interfaces where there is a large difference in Z. The computed scattering effects, on the other hand, which are assumed to depend upon small relative variations in Z, may be more affected by small errors in these estimates.

5.2 Reflection and transmission

As seen in figure 4.1, the reflections and shadows drawn in the simulated images seem to correspond well to those appearing in the true ultrasound images. They also resemble those produced by the previous simulation method, but at some weaker tissue interfaces the new method yields stronger and more distinct reflections which are closer to reality. This can e.g. be seen at the interface closest to the transducer, i.e. at the top of the image. The computed reflections are somewhat wider than those in the true ultrasound image, and this is due to the way reflection coefficients are computed for all points in space and not only for tissue interfaces. Since a certain number of elements both in front of and behind a given point are used in estimating the impedances Z_1 and Z_2, points close to an interface will receive a contribution from the interface resulting in too high reflection coefficients. This can be remedied by first performing an edge detection and then computing reflection coefficients only at the detected interfaces. However, accurate edge detection is in general a computationally intensive task, and this is therefore most easily implemented as a part of the preprocessing of the CT data set.

One obvious shortcoming of the simulated images is that the shadows have overly sharp edges. This happens because the simulation method operates with sound beams which are only one pixel wide and travel in straight lines, and each point in the simulated image receives information from only one such beam. As the beam hits a totally reflecting interface, all of the signal is therefore reflected and no signal is received from deeper within the body. In a real ultrasound system, on the other hand, the beams are wider, they have side lobes and they are refracted. As the main lobe of such a beam reaches a strong reflector, the side lobes may still go clear and continue deeper into the tissue, generating a signal from larger depths. However, the ultrasound scanner assumes that the beam is narrow and has traveled in a straight line, and it therefore interprets and displays the signal from the side lobes as if it originates at a point behind the reflector. Similarly, a beam sent out towards a reflector may be refracted and go clear, thus creating a signal which appears to originate behind the reflector. Whereas keeping track of the refracted components of the transmitted wave is complicated and not easily done within the chosen model, signal from side lobes can be implemented rather directly by adding a contribution from adjacent data points to each of the computed signals. In practice, this implies a simple smoothing of the simulated image and should be feasible to implement in real time.

Another discrepancy between the simulation and the true ultrasound image, is the reverberations. In the ultrasound image in figure 4.1(f) the reverberations can be seen as small, bright artifacts within the shadow on the left. The shadow is caused by a strong reflector close to the ultrasound transducer, and the artifacts are actually repetitions of the reflection from the upper part of this reflector. This part is perpendicular to the ultrasound beams and therefore directs most of the reflected wave energy back towards the transducer. The resulting reflections are thus much stronger than those caused by other parts of the reflector, and this is what brings about the reverberations. The variation in intensity across the reflection is not easily seen in the ultrasound images, but this is mostly due to the logarithmic compression and display evening out the signal and cutting off the peaks.

In the simulated image in figure 4.1(b), on the other hand, the corresponding reverberations appear quite different. These artifacts are considerably stronger than the true reverberations, and the first one of them is almost an exact copy of the original reflection. The apparent reason for this is that the computation of the simulated reflections is not sufficiently dependent on the orientation of the reflecting interface, and reflections which are not perpendicular to the ultrasound beams thus become too strong. As in the case of the real ultrasound image, this does not affect the appearance of the reflections in the final image significantly. However, in the case of the strong reflector in figure 4.1(b), it implies that reflections from all parts are given almost the same magnitude, thus contributing equally to the reverberations. This can be corrected by assessing the orientation of the reflecting interfaces as a part of the reflection computation, e.g. by means of a gradient estimation. The reflections from interfaces which are not perpendicular to the ultrasound beam can then be appropriately attenuated so that they do not produce any reverberations. Once again, the main challenge here is the efficiency of the required gradient estimation, as this must be performed in real time upon extracting the appropriate CT slice.

5.3 Scattering

Modern ultrasound systems are able to detect the weak, scattered signal from soft tissue structures within the human body, and this ability is an essential feature of these systems [51]. Realistic reproduction of scattering effects is therefore crucial to ultrasound simulation. However, the soft tissue components of the simulated images in figures 4.1(a)–(b) are not very similar to those seen in the corresponding true ultrasound images. The characteristic texture is quite well recreated, but hardly any of the soft tissue structures of the imaging phantom are visible. On this point, the images in figures 4.1(c)–(d) produced by the previous simulation method is closer to reality. The applied physical model describing the scattering effects predicts a quadratic relationship between the relative variations in acoustic impedance Z and the backscattered intensity I_s. In figure 5.1(c), the impedances Z computed from CT numbers along a line in the extracted CT slice shown in figure 5.1(b) are plotted versus depth r. The computed median values, used to approximate the local average Z_0, are also given in the same plot, and the corresponding relative variation $\Delta Z/Z_0$ is shown in figure 5.1(d). It is evident from these graphs that the light areas of high backscattered intensity in the ultrasound image in figure 5.1(a) correspond to somewhat elevated CT numbers in figure 5.1(b) and impedances in figure 5.1(c). However, the computed relative variations in figure 5.1(d) are quite constant, or at least not correlated with Z, and the simulation method therefore fails to reproduce these high intensities.

The reason for this failure is not obvious, but there are several possibilities. First of all, the derived scattering model forming the basis for the method is very simplified, and it is possible that it therefore neglects important effects with significant contributions to the total scattering. Simplifications such as linearization and the Born approximation are in this context good since neither higher order effects nor multiple scattering is significant in ordinary B-mode imaging [44]. The assumption of plane, harmonic incident waves, on the other hand, is not realistic. The sound field applied in B-mode imaging is a small

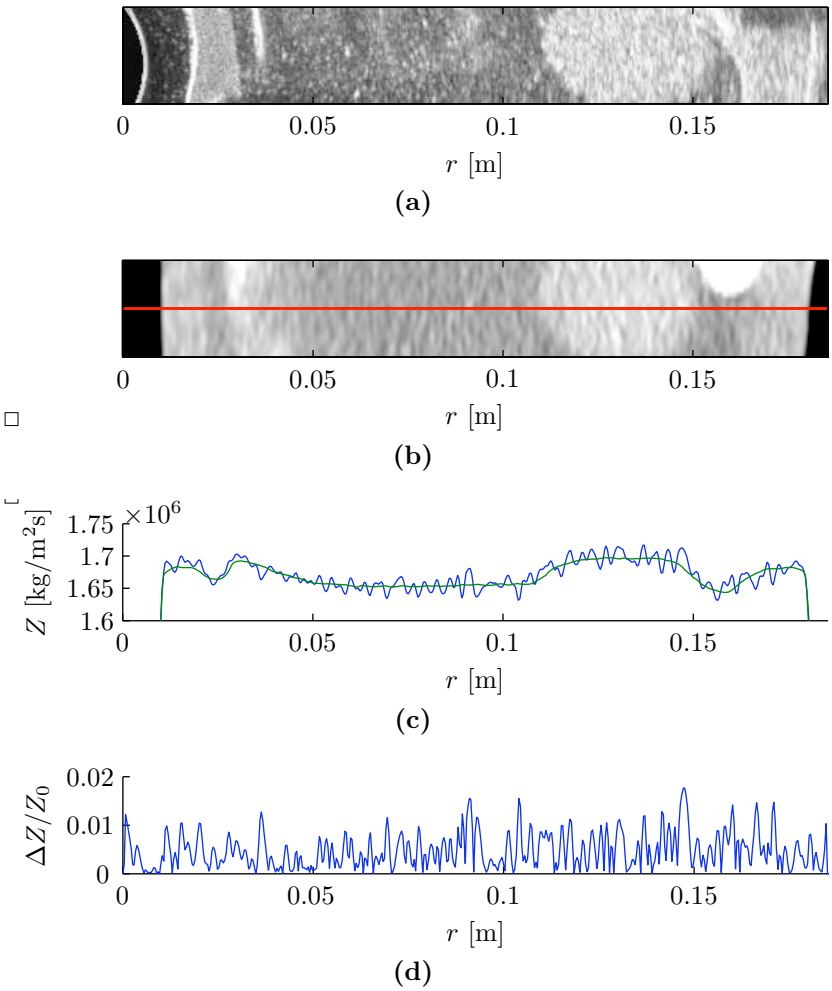

Figure 5.1: (a) A section of an ultrasound image taken from a multi-modality imaging phantom, and (b) a CT image of the same section where the midline is marked off (in red). The x-axes show distance r from the ultrasound transducer. The estimated impedance Z along the indicated midline are plotted in figure (c) (in blue) together with the median values used to approximate the local average Z_0 (in green). The variation in Z relative to Z_0 can be calculated as $\Delta Z/Z$, where $\Delta Z = Z - Z_0$. This quantity is plotted in figure (d).

pulse consisting of a main lobe and several side lobes with varying intensities, the shape of which varies with both distance from and angle to the transmitting aperture. These variations are responsible for artifacts and noise in ultrasound images, and the implemented model does not take these effects into account. Nonetheless, adjacent points in space interrogated by two consecutive pulses receive very similar amounts of energy, and the backscattered energy should therefore not be significantly affected by the explicit shape of the emitted pulse.

Now, assuming that the given model is sufficiently accurate to predict the backscattered intensities within reasonable limits, the result still depends on the input, i.e. the available information about relative variations in impedance. As discussed in section 5.1, the calculation of impedance from CT numbers is not exact, particularly since any variation in compressibility κ is ignored, and it is conceivable that small, but essential, variations in Z are neglected in this process. Yet more fundamental is the question of whether or not the required information is contained in the CT data at all. Scattering is caused by inhomogeneities on the scale of a wavelength, and for B-mode imaging this is typically between 0.2 and 0.8 mm. Modern, high-end CT scanners can produce images with an isotropic resolution below 0.4 mm [52], and they are therefore capable of resolving such inhomogeneities. However, the presented simulation method is supposed to be applied to data sets collected in various clinical settings, and the actual resolution of a given set is very much dependent upon the acquisition protocol being used. The protocols are in general designed to achieve sufficient, but not necessarily optimal, image quality for the given application while at the same time minimizing risk factors such as radiation dose. CT examinations of abdominal trauma, for instance, are routinely saved with a slice thickness of 5 mm [53, 54], and slices obtained from such data sets will not contain accurate information about the scattering inhomogeneities.

The scatterers in question are not only small in extent, but also in amplitude. Another important factor affecting the available information is therefore the contrast resolution of the CT images. CT scanners are in general quite good at resolving small variations in mass and electron densities [55]. However, an important limitation on this ability is the noise level of the system. This is usually measured by scanning a water bath and computing the standard deviation of the resulting values in a region of interest [55]. The noise varies a lot depending on acquisition parameters such as radiation dose and reconstruction method, but common values lie between 10 and 30 Hounsfield units [56]. Following the calculations described in section 3.1, this corresponds to impedance variations of about $0.015 \cdot 10^6 - 0.030 \cdot 10^6$ kg/m^{2}s in soft tissue, and variations smaller than this can thus not be distinguished from the noise in the final CT image. Considering the variations in impedance in figure 5.1(c), which is a line extracted from a typical CT data set, the local variations are only sporadically larger than the indicated noise level, and it is hence likely that most of these variations can be attributed to noise. Since this is a characteristic of the imaging system and not the imaged medium, it would explain why the computed scattering is mostly invariant throughout the simulated image except for the $1/r^2$ dependence.

Even though the available information is not sufficient to predict the ultrasound scattering by means of the presented physical model, there is, as mentioned, an apparent correspondence between CT numbers and scattered intensity in ultrasound images. This correspondence is exploited in the previously

implemented simulation method, where scattered intensity simply is given as a scaled version of the soft tissue components of the CT data. The result can be seen in figures 4.1(c)–(d). The correspondence is clearly incomplete since there are many structures within the human body not conforming to it. A typical example is blood vessels: blood has a mass density close to that of soft tissue, but it is also relatively homogeneous containing relatively few scatterers. A bloodstream will therefore have CT numbers close to those of the surrounding structures, while it will appear dark in an ultrasound image. Injection of CT contrast agents, which is common in many clinical applications [53], makes this particular discrepancy even more pronounced as it leads to a dramatic increase in the CT numbers of blood without affecting its sound scattering properties. Nonetheless, the observed correspondence is interesting, and as it is not accounted for by the simplified model presented in this work, a further investigation into the matter is pertinent.

If indeed it is the case that the information contained in the CT data is insufficient to predict the ultrasound scattering, the required information must be added. One way of doing this is to identify the different kinds of anatomical structures such as various organs, connective tissues and layers of fat in the data set and then assign a typical backscatter coefficient to each of them. It would also be possible to include other typical properties, e.g. speed of sound and compressibility, which could then be used to improve the previously discussed impedance estimates. The process of identifying spatial structures within a three-dimensional data set is known as image segmentation [6], and in the case of CT images of the human body this is a comprehensive task. However, there exist a number of both computer assisted and computer automated segmentation methods which can be applied [57], and it should therefore be feasible to implement this as a part of the preprocessing of the CT data.

5.4 Other effects

There are three elements in the presented simulation method which contribute to an attenuation of the simulated ultrasound signal: the transmission coefficients $T^{i,j}$, the absorption factor $e^{-\alpha_I r}$ and the $1/r^2$ dependence of the scattering computations. The attenuation increases with depth, and the effect on the simulated image can clearly be seen in figure 4.2(a). However, as in true ultrasound systems, the attenuation is largely counteracted by the time gain compensation (TGC) resulting in the relatively even intensities seen in 4.2(b).

The electronic noise level of ultrasound systems vary a lot, and it is therefore not easy to determine what is a typical noise level. Figures 4.1(b)–(d) show simulations with different noise levels. With a signal-to-noise ratio of 70 dB most of the actual ultrasound signal drowns in noise, while at 100 dB the noise falls outside of the dynamic range of the display and is hence not visible at all. The original simulation, with a signal-to-noise ratio of 85 dB, seems to correspond well to what is seen in the true ultrasound image. As opposed to the acoustic signal, the noise is independent of depth, and the TGC therefore causes the noise to increase throughout the image. This is particularly visible in the shadows and can also be seen in the true ultrasound image. The previous simulation method does not take electronic noise into consideration. Therefore, to avoid completely black shadows with a rather artificial look, the speckle

pattern is extended to also cover the shadows. However, shadows are caused by the absence of acoustic signal, including speckle signal, and the result is somewhat far from the true images.

One feature distinguishing the true ultrasound image from the simulated image is the deformation at the top which is seen in both figure 4.1(e) and figure 4.1(f). The deformation is caused by the pressure from the ultrasound probe, and since this pressure was absent during the recording of the CT data, this is not seen in the simulations. Visually, this discrepancy is not critical. However, the eye-hand coordination and the connection between tactile response and visual output is essential in operating an ultrasound scanner. The deformations are therefore not unimportant. Simulation methods taking such features into account have previously been developed [58, 59], and these techniques can readily be adapted to the method presented here.

5.5 Speed and application to clinical CT data

Since the simulation method presented here is intended used in a training simulator, it must be capable of delivering simulated images at a frame rate comparable to that of a true ultrasound scanner, i.e. about 10 frames per second. This is approximately 10 times faster than what is accomplished by the new simulation method at the present time. Even though the real time constraint formed the basis for the development of the method, the focus of this master's project has been the realism of the simulated images rather than the speed of the simulations. The current implementation is therefore not optimal, particularly with respect to the handling and storage of the processed CT data. However, the computational principles which have been implemented are all suited for fast execution. Several operations, such as the computation of impedances and average impedances, can be performed as a part of the preprocessing of the CT data. The absorption factors and speckle pattern are similarly only dependent on scan sector geometry and need only be updated whenever these settings are changed. This leaves only a few operations which depend on the position and orientation of the scan sector and therefore must be performed in real time. This includes the extraction of the appropriate scan sector from the three-dimensional CT data, the calculations of reflection and transmission coefficients and reverberations and the final scan conversion of the simulated image. These are all relatively fast computations which should be possible to perform with a frame rate close to real time.

Another challenge is that the simulation method is meant to be applied to CT data collected from human beings in actual, clinical settings. So far it has only been tested on data taken from a multi-modality imaging phantom, and even though this is made to imitate the properties of the human body under both CT and ultrasound imaging, there are many differences. First of all, the phantom contains only a few, well defined structures, each with a determinate set of properties. The composition of human tissue is in general more varied, and computations which function appropriately for the interfaces encountered in the phantom may prove to fail for other and more complex interfaces. Moreover, CT images of patients taken in clinical settings may be more exposed to noise than images of a phantom. Even though parts of the presented method seem to work well for the phantom data, further testing with clinical data is therefore

necessary.

5.6 Future work

Several parts of the new simulation method show promise, and in the previous sections, many possible improvements have already been suggested. The computed reflections and reverberations can e.g. be made more realistic by limiting the computations to identified tissue interfaces and taking the direction of these interfaces into account. The obvious challenge is the real time constraint which implies that the process of finding and analyzing these interfaces must either be performed very fast or be done in advance. The last option also requires the results to be stored in an efficient manner. New effects, such as side lobe artifacts and tissue deformation, can also be included in the simulations.

The developed physical model failed to predict scattering effects based on the available CT data, and the apparent connection between CT numbers and the intensity in ultrasound images should therefore be investigated further. One possibility is here to perform some sort of regression analysis based on representative CT and ultrasound data sets as indicated by Wein et al. [39]. However, it is likely that CT data on its own do not contain sufficient information, and the possibility of adding information, e.g by means of segmentation, should therefore also be considered.

The current implementation of the simulation method is relatively slow, but it has as mentioned a significant potential for improvements. By optimizing data handling and processing, it should be possible to achieve real time performance. Finally, as tests on phantom data show satisfactory results, the new method should be tested on CT data recorded from humans. By also recording true ultrasound images corresponding to these CT data, a direct and intuitive evaluation of the realism of the simulations can be performed using the presented experimental setup.

Chapter 6

Conclusion

An ultrasound simulation method has been developed producing artificial ultrasound images based on three-dimensional CT data sets. It utilizes quantitative information in the CT data to estimate acoustic impedance values, and it combines this with physical models connecting the estimates to effects fundamental to ultrasound image formation, mainly reflection and scattering. The method is designed to allow simulation in real time, and it is likely that this can be achieved by optimization of the implementation.

Simulated images produced by the new method have been presented and compared to corresponding true ultrasound images as well as to images produced by a previously developed method. The comparisons show that the reflections and shadows simulated by the new method correspond well to those seen in the true ultrasound images, and they are also slightly more realistic than those produced by the previous method. This indicates that such computations can benefit from taking quantitative information into account. The implementation of effects such as absorption and electronic noise further adds to the realism of the simulations. However, the attempt at computing ultrasound scattering based on CT data was not successful, and it is likely that CT images, particularly if recorded in clinical settings, do not contain sufficient information to act as a basis for simulation of such effects. Alternative methods should therefore be considered for this purpose.

Bibliography

[1] Neville Stanton. Simulators: a review of research and practice. In Neville Stanton, editor, *Human Factors in Nuclear Safety*. CRC Press, 1996.

[2] Richard M. Satava. Accomplishments and challenges of surgical simulation. *Surgical Endoscopy*, 15(3):232–241, 2001.

[3] Michael L. Good. Patient simulation for training basic and advanced clinical skills. *Medical Education*, 37(s 1):14–21, 2003.

[4] David J. Vining, David R. Stelts, David K. Ahn, Paul F. Hemler, Yaorong Ge, Gordon W. Hunt, Christopher Siege, Daniel B. McCorquodale, Mark E. Sarojak, and Gilbert R. Ferretti. Freeflight: A virtual endoscopy system. In Jocelyne Troccaz, Eric Grimson, and Ralph Mösges, editors, *CVRMed-MRCAS' 97. First Joint Conference. Computer Vision, Virtual Reality and Robotics in Medicine and Medical Robotics and Computer-Assisted Surgery. Proceedings*, volume 1205 of *Lecture Notes in Computer Science*, pages 413–416, Grenoble, France, 1997.

[5] H. Maul, A. Scharf, P. Baier, M. Wuestemann, HH Guenter, G. Gebauer, and C. Sohn. Ultrasound simulators: experience with the sonotrainer and comparative review of other training systems. *Ultrasound in Obstetrics and Gynecology*, 24(5):581–585, 2004.

[6] Jerrold T. Bushberg. *The Essential Physics of Medical Imaging*. Lippincott Williams & Wilkins, Philadelphia, PA, USA, second edition, 2002.

[7] Bjørn A. J. Angelsen. Principles of medical ultrasound imaging and measurements. In *Ultrasound Imaging. Waves, signals and signal processing*, volume 1. Emantec, Trondheim, Norway, 2000.

[8] Bjørn A. J. Angelsen. Introduction. In *Ultrasound Imaging. Waves, signals and signal processing*, volume 1. Emantec, Trondheim, Norway, 2000.

[9] K. Kirk Shung. Introduction. In K. Kirk Shung and Gary A. Thieme, editors, *Ultrasonic Scattering in Biological Tissues*. CRC Press, Boca Raton, FL, USA, 1993.

[10] Jørgen Arendt Jensen. Ultrasound imaging and its modeling. In Mathias Fink, editor, *Imaging of Complex Media with Acoustic and Seismic Waves*, volume 84 of *Topics in Applied Physics*, pages 135–166. Springer, Berlin, Germany, 2002.

[11] B. Breyer, C. A. Bruguera, H. A. Gharbi, B. B. Goldberg, F. E. H. Tan, M. W. Wachira, and F. S. Weill. *Manual of diagnostic ultrasound*. World Health Organization, Geneva, Switzerland, 1995.

[12] Steven A. Godwin. Introduction to emergency ultrasound. *Jacksonville Medicine Magazine*, 50(3), 1999.

[13] Lars Eirik Bø. Experimental setup for evaluation of ultrasound simulation method. Technical report, Department of Mathematical Sciences, Norwegian University of Science and Technology, 2007.

[14] R. Lerch. Simulation of piezoelectric devices by two- and three-dimensional finite elements. *IEEE Transactions on Ultrasonics, Ferroelectrics and Frequency Control*, 37(3):233–247, 1990.

[15] Jørgen Arendt Jensen. Simulation of advanced ultrasound systems using field ii. In *Proceedings of the 2004 IEEE International Symposium on Biomedical Imaging: From Nano to Macro*, pages 636–639, Arlington, VA, USA, 2004.

[16] D. d'Aulignac, C. Laugier, J. Troccaz, and S. Vieira. Towards a realistic echographic simulator. *Medical Image Analysis*, 10(1):71–81, 2006.

[17] Rafael Domínguez-Castro. Solving spice problems. *IEE Proceedings G – Circuits, Devices and Systems*, 135(4):177–178, 1988.

[18] S. Sherrit, H. D. Wiederick, B. K. Mukherjee, and M. Sayer. An accurate equivalent circuit for the unloaded piezoelectric vibrator in the thickness mode. In S. C. Schneider, M. Levy, and B. R. McAvoy, editors, *1997 IEEE Ultrasonics Symposium. Proceedings*, volume 2, pages 2354–2363, Toronto, Ont., Canada, 1997.

[19] Stewart Sherrit, Sean P. Leary, Benjamin P. Dolgin, and Yoseph Bar-Cohen. Comparison of the Mason and KLM equivalent circuits forpiezoelectric resonators in the thickness mode. In S. C. Schneider, M. Levy, and B. R. McAvoy, editors, *1999 IEEE Ultrasonics Symposium. Proceedings*, volume 2, pages 921–926, Caesars Tahoe, NV, USA, 1999.

[20] Gerald R. Harris. Review of transient field theory for a baffled planar piston. *The Journal of the Acoustical Society of America*, 70(1):10–20, 1981.

[21] Geoff E. Tupholme. Generation of acoustic pulses by baffled plane pistons. *Mathematika*, 16(209–224), 1969.

[22] Peter R. Stepanishen. The time-dependent force and radiation impedance on a piston in a rigid infinite planar baffle. *The Journal of the Acoustical Society of America*, 49(3):841–849, 1971.

[23] Peter R. Stepanishen. Transient radiation from pistons in an infinite planar baffle. *The Journal of the Acoustical Society of America*, 49(5):1629–1638, 1971.

[24] Jørgen Arendt Jensen and Niels Bruun Svendsen. Calculation of pressure fields from arbitrarily shaped, apodized, and excited ultrasound transducers. *IEEE Transactions on Ultrasonics, Ferroelectrics, and Frequency Control*, 39:262–267, 1992.

[25] Jørgen Arendt Jensen. Field: A program for simulating ultrasound systems. *Medical and Biological Engineering and Computing*, 34((sup. 1)):351–353, 1997.

[26] T. Douglas Mast, Laurent P. Souriau, D.-L. Donald Liu, Makoto Tabei, Adrian I. Nachman, and Robert C. Waag. A k-space method for large-scale models of wave propagation in tissue. *IEEE Transactions on Ultrasonics, Ferroelectrics and Frequency Control*, 48(2):341–354, 2001.

[27] Trond Varslot, Gunnar Taraldsen, Tonni F. Johansen, and Bjørn A. J. Angelsen. Computer simulation of forward wave propagation in non-linear, heterogeneous, absorbing tissue. *2001 IEEE Ultrasonics Symposium*, 2: 1193–1196, 2001.

[28] Alexander I. Veress, W. Paul Segars, Jeffrey A. Weiss, Benjamin M. W. Tsui, and Grant T. Gullberg. Normal and pathological NCAT image and phantom data based on physiologically realistic left ventricle finite-element models. *IEEE Transactions on Medical Imaging*, 25(12):1604–1616, 2006.

[29] Jørgen Arendt Jensen and Peter Munk. Computer phantoms for simulating ultrasound B-mode and CFM images. *Acoustical Imaging*, 23:75–80, 1997.

[30] Jørgen Arendt Jensen and Svetoslav Ivanov Nikolov. Fast simulation of ultrasound images. In S. C. Schneider, M. Levy, and B. R. McAvoy, editors, *2000 IEEE Ultrasonics Symposium. Proceedings*, volume 2, pages 1721–1724, San Juan, Purto Rico, 2000.

[31] Hans Torp, Tonni Johansen, and Jo Stein Haugen. Nonlinear wave propagation – a fast 3D simulation method based on quasi-linear approximation of the second harmonic field. *2002 IEEE Ultrasonics Symposium*, 1:567–570, 2002.

[32] E. Varlet. *Etude d'un simulateur pedagogique d'écho-endoscopie digestive, modélisation et réalisation.* PhD Thesis, Université de Lille, 1997.

[33] Ciamak Abkai, Nico Becherer, Jurgen Hesser, and Reinhard Manner. Real-time simulator for intravascular ultrasound (IVUS). In Stanislav Y. Emelianov and Stephen A. McAleavey, editors, *Medical Imaging 2007: Ultrasonic Imaging and Signal Processing*, volume 6513 of *Proceedings of SPIE*, page 65131E, San Diego, CA, USA, 2007.

[34] Isabelle Fontaine, Michel Bertrand, and Guy Cloutier. A system-based approach to modeling the ultrasound signal backscattered by red blood cells. *Biophysical Journal*, 77(5):2387–2399, 1999.

[35] Dror Aiger and Daniel Cohen-Or. Real-time ultrasound imaging simulation. *Real-Time Imaging*, 4(4):263–274, 1998.

[36] Hans-Heino Ehricke. SONOSim3D: a multimedia system for sonography simulation and education with an extensible case database. *European Journal of Ultrasound*, 7(3):225–230, 1998.

[37] Michael Weidenbach, Florentine Wild, Kathrin Scheer, Gerhard Muth, Stefan Kreutter, Garnoth Grunst, Thomas Berlage, and Peter Schneider. Computer-based training in two-dimensional echocardiography using an echocardiography simulator. *Journal of the American Society of Echocardiography*, 8:362–366, 2005.

[38] Alexandre Hostettler, Clément Forest, Antonello Forgione, Luc Soler, and Jacques Marescaux. Real-time ultrasonography simulator based on 3D CT-scan images. *Studies in Health Technology and Informatics*, 111:191–193, 2005.

[39] Wolfgang Wein, Ali Khamene, Dirk-André Clevert, Oliver Kutter, and Nassir Navab. Simulation and fully automatic multimodal registration of medical ultrasound. In Nicholas Ayache, Sébastien Ourselin, and Anthony Maeder, editors, *Medical Image Computing and Computer-Assisted Intervention — MICCAI 2007*, volume 4791, pages 136–143, Brisbane, Australia, 2007.

[40] Marcelo Alonso and Edward J. Finn. *Pysics*. Addison Wesley, Harlow, England, first edition, 1992.

[41] Wilfried Schneider, Thomas Bortfeld, and Wolfgang Schlegel. Correlation between CT numbers and tissue parameters needed for Monte Carlo simulations of clinical dose distributions. *Physics in Medicine and Biology*, 45 (2):459–478, 2000.

[42] Simon A. Jackson and Richard M. Thomas. *Cross-sectional Imaging Made Easy*. Churchill Livingstone, Edinburgh, 2005.

[43] Martin E. Anderson and Gregg E. Trahey. A seminar on k-space applied to medical ultrasound, 2006.
http://dukemil.egr.duke.edu/Ultrasound/k-space/bme265.pdf (2007-12-12).

[44] Michael F. Insana and David G. Brown. Acoustic scattering theory applied to soft biological tissues. In K. Kirk Shung and Gary A. Thieme, editors, *Ultrasonic Scattering in Biological Tissues*. CRC Press, Boca Raton, FL, USA, 1993.

[45] Bjørn A. J. Angelsen. Waves in homogeneous tissue. In *Ultrasound Imaging. Waves, signals and signal processing*, volume 1. Emantec, Trondheim, Norway, 2000.

[46] Robert C. McOwen. *Partial differential equations: methods and applications*. Pearson Education, Inc., Upper Saddle River, NJ, USA, second edition, 2003.

[47] Adrian I. Nachman, James F. III Smith, and Robert C. Waag. An equation for acoustic propagation in inhomogeneous media with relaxation losses. *The Journal of the Acoustical Society of America*, 88(3):1584–1595, 1990.

[48] Ralph J. Smith. *Electronics: circuits and devices*. John Wiley & Sons, New York, NY, USA, third edition, 1987.

[49] David P. Shattuck, Marc D. Weinshenker, Stephen W. Smith, and Olaf T. von Ramm. Explososcan: A parallel processing technique for high speed ultrasound imaging with linear phased arrays. *The Journal of the Acoustical Society of America*, 75(4):1273–1282, 1984.

[50] *Interventional 3D abdominal phantom*. Computerized Imaging Reference Systems, Inc., Norfolk, Virginia, USA, 2007.
http://www.cirsinc.com/pdfs/057cp.pdf (2007-11-28).

[51] Gary A. Thieme. Clinical relevance of scattering. In K. Kirk Shung and Gary A. Thieme, editors, *Ultrasonic Scattering in Biological Tissues*. CRC Press, Boca Raton, FL, USA, 1993.

[52] Elliot K. Fishman. Cardiac CT: Where are we today and where are we going? *Supplement to Applied Radiology*, 35(12):5–9, 2006.

[53] W. Richard Webb, Nancy M. Major, and William E. Brant. *Fundamentals of body CT*. Saunders Elsevier, Philadelphia, PA, USA, third edition, 2006.

[54] Robert A. Novelline. Total body trauma scanning with 64-slice scanner. In *International imaging course 07*, pages 2–3, Hong Kong, China, 2007.

[55] Stewart C. Bushong. *Radiologic science for technologists: physics, biology, and protection*. Elsevier Mosby, St. Louis, MO, USA, eighth edition, 2004.

[56] Kirsten L. Boedeker, Virgil N. Cooper, and Michael F. McNitt-Gray. Application of the noise power spectrum in modern diagnostic mdct: part i. measurement of noise power spectra and noise equivalent quanta. *Physics in medicine and biology*, 52:4027–4046, 2007.

[57] Dzung L. Pham, Chenyang Xu, and Jerry L. Prince. Current methods in medical image segmentation. *Annual Review of Biomedical Engineering*, 2 (1):315–337, 2000.

[58] Ron Alterovitz, Jean Pouliot, Richard Taschereau, I-Chow Joe Hsu, and Ken Goldberg. Simulating needle insertion and radioactive seed implantation for prostate brachytherapy. *Medicine Meets Virtual Reality*, 11:19–25, 2003.

[59] Jocelyne Troccaz, Delphine Henry, Noureddine Laieb, Guillaume Champleboux, Jean-Luc Bosson, and Olivier Pichot. Simulators for medical training: application to vascular ultrasound imaging. *The Journal of Visualization and Computer Animation*, 11:51–65, 2000.